Molecular Dynamics Simulations of Non-Photochemical Laser-Induced Nucleation

Electrolyte Clustering by Nanoparticle Heating

T.P. van Waas

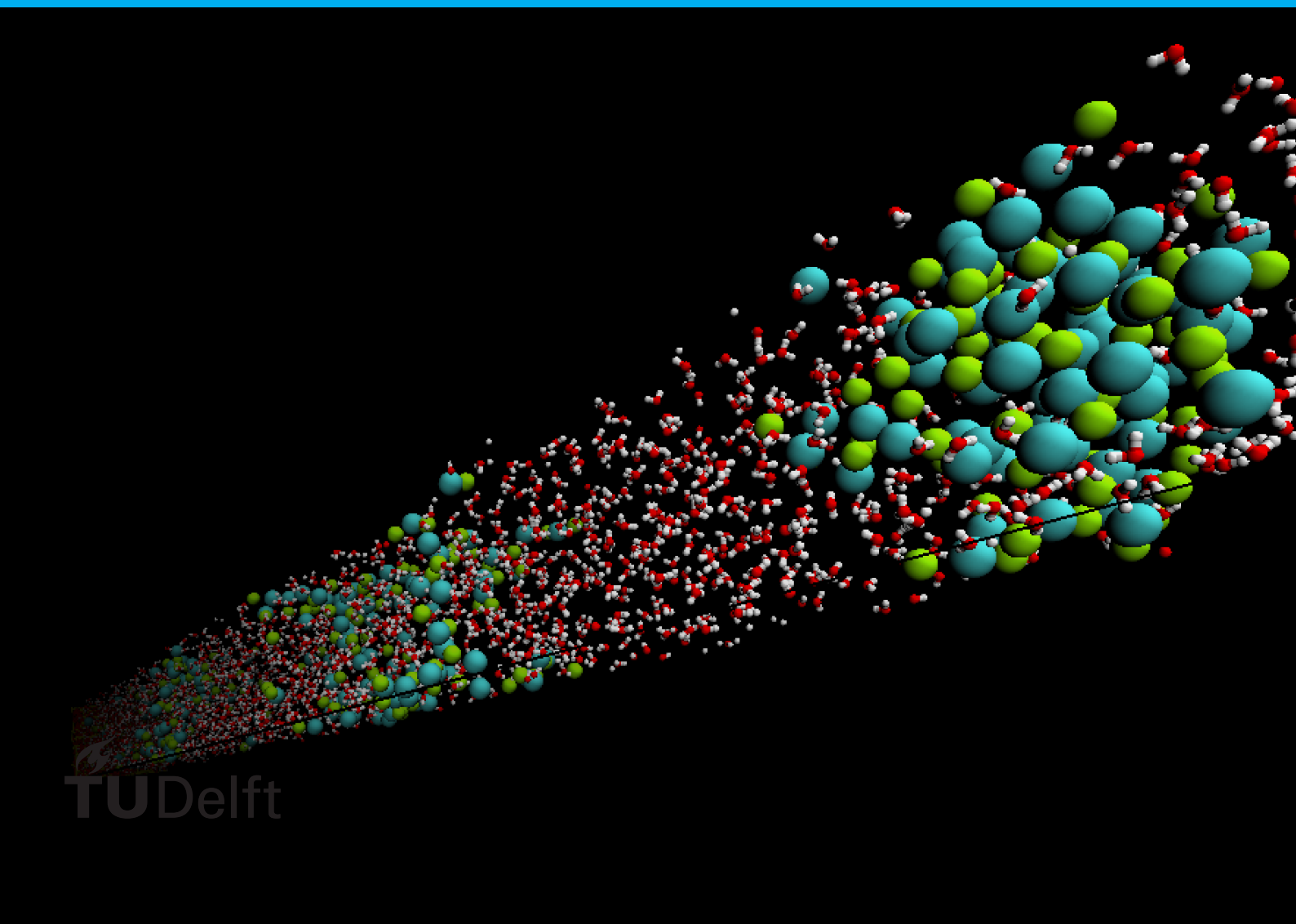

TU Delft

Molecular Dynamics Simulations of Non-Photochemical Laser-Induced Nucleation

Electrolyte Clustering by Nanoparticle Heating

by

T.P. van Waas

In partial fulfillment of the degree of
Bachelor of Science Applied Physics
at Delft University of Technology,
to be defended publicly on Monday October 14, 2019 at 10:00 a.m..

Student number:	4515560	
Project duration:	April 22, 2019 – October 14, 2019	
Under guidance and supervision of:	Dr. R.M. Hartkamp,	TU Delft, daily supervisor
	Dr. J.M. Thijssen,	TU Delft, supervisor
Thesis committee:	Dr. R.M. Hartkamp,	TU Delft, daily supervisor
	Dr. J.M. Thijssen,	TU Delft, supervisor

This thesis is confidential and cannot be made public until October 14, 2019.

An electronic version of this thesis is available at http://repository.tudelft.nl/.

Cover image: Visualisation of clustering of K^+ and Cl^- ions in a water column with periodic lateral faces. The image was created using the Visual Molecular Dynamics software [1].

TU Delft

Preface

Sources

This thesis is the second thesis by the author on the subject of non-photochemical laser-induced nucleation. Even though the first thesis [2] is based on experimental work and the second thesis is based on simulations, some concepts are discussed in both papers. In particular, the concepts on NPLIN and its mechanisms found in Chapter 1 and Chapter 2 have been discussed previously. In an attempt to uphold good scientific practice, all attempts have been made to avoid self-plagiarism, in particular by paraphrasing and citing original literature.

Acknowledgements

Abstract

Non-photochemical laser-induced nucleation (NPLIN) is a process where a crystalline phase is formed out of solution by exposure to a laser beam. In NPLIN, the nucleation probability is strongly dependent on the beam intensity and weakly dependent on the wavelength. NPLIN offers a feasible alternative to energy-intensive industrial crystallisation methods. Although several mechanisms have been proposed, little is known about NPLIN at the molecular level. Some theories suggest that nucleation rates are enhanced through the heating of nanoparticles by absorption of electromagnetic energy. In this work, molecular dynamics simulations are performed on the clustering of ions in the vicinity of a heated nanoparticle in an aqueous supersaturated KCl solution. The spherical symmetry of a spherical nanoparticle in solution is exploited by modelling a laterally periodic water column of an initial length of 500 Å enclosed between a planar Fe_2O_3 nanoparticle surface and a graphene layer acting as a piston. A cavitation bubble is formed after nanoparticle heating, leading to an increase of clustered ions according to a bond order criterion. Because the clusters satisfy satisfy $\Delta G < 0$ for locally valid NPT ensembles, crystallisation is predicted by the mechanism for experimental systems. The results corroborate concentration based NPLIN mechanisms as the clustering is visibly induced by local solute evaporation. Pressure based mechanisms appear ineffective because no effects of pressure waves are observed. Thermostatting the graphene layer does not yield observable dissipation of the thermal energy generated through the nanoparticle heating and at the ion clustering sites, obstructing completion of the cavitation cycle at a feasible simulation duration. It is suggested to repeat the simulations using a system in the shape of a cone and a piston of higher transverse thermal conductivity.

Contents

1 Introduction

1.1. Relevance

Crystallisation is a process defined as the formation of a solid where the constituent atoms or molecules move into a highly organised structure known as a crystal [3]. Crystallisation is an ubiquitous method in chemical engineering, involving large amounts of energy and waste per amount of product [4]. Crystallisation is employed at large scales in chemical industries, where the crystallisation is often initiated by evaporation of the solvent or cooling of the solution.

Crystallisation occurs in two steps. The first step is nucleation, where a distinct solid phase is formed out of constituent particles. The second step is crystal growth, where the formed nuclei increase in size through accretion of new particles. Nucleation can be further divided into primary nucleation, being the formation of the first nuclei, and secondary nucleation, which is the growth of existing nuclei into observable crystals. Primary nucleation is denoted as heterogeneous when formed due to a phase distinct from the solution, or homogeneous without any influence of the distinct phase.

In 1996, Garetz *et al.* discovered that exposing supersaturated solutions to a laser beam could decrease the crystallisation induction times by $O(10^6)$ [5, 6]. The effect was coined non-photochemical laser-induced nucleation (NPLIN). Because of a strong dependence on intensity and weak dependence on wavelength found in the experiments, it is likely that NPLIN is distinct from photochemical laser-induced nucleation, which relies on the quantisation of electron excitations [7]. NPLIN appears to induce primary nucleation and it proposes a fast and energy efficient alternative to current crystallisation methods [8].

In the literature, several mechanisms have been described to explain the phenomena of NPLIN [8, 9]. These mechanisms can be divided into three types, dependent on how the laser beam can interact with the sample. As the laser beam is an electromagnetic wave, it can interact through the material through i) its magnetic field, ii) its electric field and iii) absorption of electromagnetic energy. As most studied systems are hardly affected by magnetic fields, no conventional NPLIN mechanisms rely on effects solely based on the magnetic field [8]. By contrast, a fair share of the mechanisms are based on interactions between the electric field and the material. Moreover, it has been found that migration of particles due to a static electric field yields insignificant increases in nucleation rates for systems prone to NPLIN [10]. Therefore, mechanisms based on the electric field generally address the change in relative stability of phases during exposure to the laser beam [9]. In the theories based on the absorption of electromagnetic energy, it is noted that significant amounts of energy are absorbed by nanoparticles in the solution [11], which may explain the weak wavelength dependence and the strong intensity dependence. The nanoparticle based mechanisms can be investigated by modelling and simulating a system containing a nanoparticle and a solution containing particle types which have been crystallised experimentally using NPLIN.

1.2. Crystallisation thermodynamics and NPLIN

In classical nucleation theory (CNT), the Gibbs energy ΔG of the formation of a crystal for homogeneous nucleation is given as:

$$\Delta G = A\sigma + V\rho\Delta\mu, \tag{1.1}$$

where A is the interface area of the formed nucleus, σ is the interfacial tension, V is the volume of the formed crystal, ρ is the particle density in the crystal and $\Delta\mu = \mu_s - \mu_l$ is the change of chemical potential from the liquid to the solid phase. Additionally, $\Delta\mu$ may be regarded as the driving term, invoking formation of crystals from solution. Due to a low surface to volume ratio, it is often assumed that the particles will obtain a spherical shape, such that ΔG becomes

$$\Delta G(r) = 4\pi r^2\sigma + \frac{4}{3}\pi r^3 \rho \Delta\mu. \tag{1.2}$$

By taking the derivative in Equation 1.2 and equating it to 0, the maximum in the Gibbs energy is found at the critical radius r_c:

$$r_c = -\frac{2\sigma}{\rho\Delta\mu}, \tag{1.3}$$

from which it follows that primary nuclei will form with a radius $r \geq r_c$. In this paper, ion clusters of a geometry having $\Delta G(r > r_c)$ will be denoted as *subcritical* and of a geometry having $\Delta G(r < r_c)$ will be denoted as *supercritical*. The dependence of σ and $\Delta\mu$ on the solution temperature and concentration give rise to phase diagrams for particular solutes, as displayed in Figure 1.1.

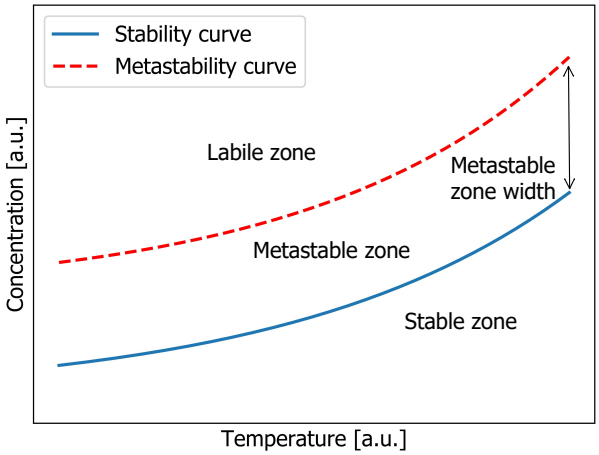

Figure 1.1: An idealised phase diagram for a solute. In the stable zone, solutes will always dissolve. In the metastable zone, there is crystal growth but no spontaneous nucleation. In the labile zone, both crystal growth and spontaneous nucleation will occur. The metastable zone is dashed to emphasise the dependence on nucleation rates. Image obtained from van Waas [2].

Moreover, the nucleation rate according to CNT is predicted as [12]:

$$k = N_S Z_j \exp\left(\frac{-\Delta G(r_c)}{k_B T}\right) \tag{1.4}$$

where N_S is the number of nucleation sites, Z_j is the Zeldovich factor, i.e. the probability that a cluster at the critical radius will crystallise for a given rate of matter flux j, k_B is the Boltzmann constant and T is the temperature.

It has been shown experimentally that the the laser intensity threshold for nucleation of $I_{\text{nuc}} = 5.2\,\text{MW/(cm)}^2$ for various salts is remarkably close to the intensity threshold of $I_{\text{cav}} = 5.4\,\text{MW/(cm)}^2$ for the generation of so-called *cavitation bubbles* [11]. A cavitation bubble is a transient local vapour bubble within a liquid and can be caused by rapid changes in pressure or temperature [13]. In recent research, the formation of crystals in presence of laser-induced cavitation bubbles have been reported [14]. However, it is unknown where and when the nucleation occurs with respect to the cavitation bubbles.

Recently, some researchers have embarked on employing molecular dynamics (MD) to simulate certain mechanisms and processes relevant to NPLIN [15–17]. MD is a numerical simulation method for studying the physical movements of molecules and will be further explained in Chapter 2. Sindt *et al.* [15] have performed a molecular dynamics study on rapidly heating a diamond-like nanoparticle in a KCl solution. There, it is shown that heating a nanoparticle from an initial temperature of $T_{\text{i}} = 298$ K to several thousands of Kelvin leads to the clustering and structuring of K^+ and Cl^- ions using distance-based and order-based criteria, showing that nanoparticle based mechanisms are plausible at the molecular scale. However, detailed

study of the results show that certain improvements can be made. First, the nanoparticle in the paper is heated instantaneously, disregarding any equilibration time of the carbon molecules. Second, the simulations involve a carbon nanoparticle, whereas experimental work has shown that iron oxides and phosphates are the main impurities [11]. Third, the majority of the simulation time is performed in an NPH (particle-pressure-enthalphy) ensemble. As a consequence, the cubic box size increases during the simulation, thereby affecting the potential energies of the molecular configurations. Lastly, if it is assumed that the observed effects are radially symmetric, improvements in the computation times can be achieved by setting up parallel to the normal vector of the nanoparticle surface.

1.3. Molecular modelling of fluids

The conduct of science can be divided conceptually into three parts: theorising, experimentation and simulation [18]. Often, the objective of experiments and simulations is to validate models and hypotheses which have been theorised [19]. Moreover, some dangerous experiments can be simulated, providing a safe alternative. In this work, simulations are conducted on an NPLIN mechanism at the molecular level to obtain an understanding of macroscopic phenomena. The incentive is to clarify the workings at the nanoscale and to evaluate certain proposed NPLIN mechanisms. If the interpretation of the given mechanism proves reliable, the model provides a basis for simulations with different geometries, experimental conditions and solutes.

Figure 1.2 shows a conceptualisation of the simulation of liquids. The steps following the modelling of liquids will be followed in this paper. Specifically, a solution of KCl in water will be considered as the liquid as there is a large amount of literature available on NPLIN studies for KCl. A model for this system and its relation to the cavity mechanism will be provided in Chapter 2. From there, the main focus will be to perform computer simulations, while constructing approximate theories to obtain theoretical predictions. The results of the model can then be compared to the predictions and the experimental results. The results may serve as the basis for future theorising, experimentation and simulation.

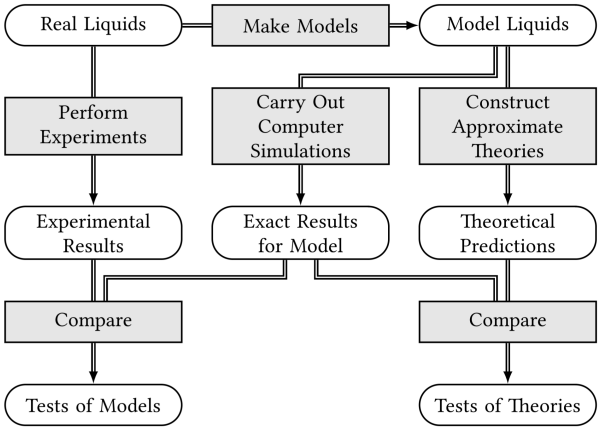

Figure 1.2: A flow diagram of a conceptualisation in the study of liquids. Image taken from Allen and Tildesley [20].

1.4. Research question

Given the current knowledge on the mechanisms of NPLIN at the molecular scale, the central research question of this paper is formulated as follows: Which of the NPLIN mechanisms agree with the clustering of ions as potentially observed in MD simulations of KCl dissolved in water in the vicinity of a heated nanoparticle? This central question should be answered by completing the following objectives:

- A model of a nanoparticle in a KCl electrolyte solution should be developed. Assumptions and approximations should be considered in view of the limited computational resources.
- The model should be used to perform molecular dynamics simulations of a KCl solution along the cavitation bubble cycle based on the heating of a nanoparticle.
- The concentration and temperature of the electrolytes should be checked as a function of position and time. In particular, it should be investigated when and where the electrolytes aggregate into clusters larger than the critical size as predicted by CNT.

2

Theory

This chapter contains the theory which is considered relevant for subsequent chapters of this paper. Section 2.1 provides an overview of relevant notions and observations in the debate of NPLIN. In Section 2.2, some important experimental observations are discussed. In Section 2.3, four proposed mechanisms of NPLIN will be discussed. The so-called cavity-induced concentration-enhanced nucleation (CICEN) mechanism will be discussed in most detail, as it is arguably the most relevant mechanism for the simulations of this paper. The simulation method of molecular dynamics (MD) and its algorithms will be discussed in Section 2.4. Two anticipated consequences of the geometry of the model are discussed in Section 2.5.

2.1. Terminology

Given a concentration as c in mass per volume or moles per volume and $c_s(T)$ as the solubility at a given temperature T, the supersaturation $S(T)$ is defined as

$$S(T) = \frac{c(T)}{c_s(T)}. \tag{2.1}$$

Typically, $S(T) \in [1, 1.10]$ for NPLIN experiments. Moreover, $S(T)$ can be regarded as a driving term for nucleation, as in the absence of pressure difference, it can be derived that [21]:

$$\Delta\mu \approx -k_B T \ln(S), \tag{2.2}$$

where k_B is the Boltzmann constant. With respect to Figure 1.1, $S(T)$ can give a direct impression of the stability of experimental samples. According to CNT, the nucleation rate k should scale linearly with $S(T)$ as k scales exponentially with $\Delta\mu$.

A unique aspect of NPLIN is that it sometimes allows for control over the morphology during crystallisation [22]. *Polymorphism* is the ability of a solid to exist in more than a single crystalline structure. Glycine has been studied thoroughly because it was conjectured that the fractions of α and γ polymorphs could be controlled through experimental conditions [8]. Initially, it was proposed that the obtained polymorph was influenced by the polarisation of the laser light, which was coined *polarisation switching* [5]. In subsequent years, polarisation switching has not been reproduced succesfully [23, 24]. Moreover, it is suggested from recent results that the morphology of the obtained crystal is dependent on $S(T)$ [22].

2.2. Experimental observations

In recent years, many experiments have been performed with respect to so-called *impurities*. As any cavitation bubbles are generated by heating these nanoparticles, these particles are indispensable for mechanisms based on absorption of electromagnetic energy. by contrast, such particles are not required in theories based on the electric component of the laser [8]. Therefore, experimenting with varying amounts of nanoparticles allows for evaluating the relevance of the two types of mechanisms. Upon using ultrapure water having a resistivity of $\rho = 18.2$ M$\Omega\cdot$ cm and precleaned vials, mass spectrometry of dry mass shows that the reported impurity amounts correlate strongly with the residues reported on sample containers of the solutes of NPLIN samples [11]. Moreover, phosphates and iron oxides such as Fe_2O_3 (hematite) are common predominant

contaminants in terms of mass. Javid *et al.* [25] have shown that nanofiltration of glycine samples suppresses nucleation attributed to the laser by nearly an order of magnitude and leaving the spontaneous nucleation rates unaltered.

The laser intensity at the nucleation site strongly determines what effects are observed [9]. At high intensities near I_{break} of $O(100\ \text{MW/(cm)}^2)$, the electromagnetic field can excite electrons from solid or fluid molecules, known as optical breakdown [26]. Such ionisation may be regarded as indirect photochemical laser-induced nucleation (PLIN). PLIN offers lower levels of spatiotemporal and morphologic control. At intensities below $I_{\text{nuc}} = 5.2\ \text{MW/(cm)}^2$ for various alkali halides [11], no increased nucleation rates are observed. Consequently, there remains an experimental intensity range between I_{nuc} and I_{break}.

2.3. NPLIN mechanisms

The first two methods of this section are based on the electric field of the laser and the latter two methods are based on nanoparticle heating through absorption of electromagnetic energy by a nanoparticle, leading to the formation of a cavitation bubble. As mentioned by van Waas [2], it is possible that observed phenomena are caused by an interplay of different mechanisms.

2.3.1. Optical Kerr effect

The optical Kerr effect (OKE) is based on the interaction between the laser electric field component and any anisotropic polarisation of molecules, such as glycine. Specifically, the polarisation should align the static polarisation of the molecules with the polarisation of the electric field, thus changing the orientation of the crystalline arrangement. As experiments were performed with different light polarisations, it was conjectured initially that different crystal morphologies could be observed through alignment between light polarisation and anisotropic polarisation [27]. In what is commonly known is the OKE in physics, the laser irradiance locally alters the refractive index of the material dependent on the polarisation of light [28]. The NPLIN OKE is analogous to the physical OKE because it aligns the molecules through their static dipoles along certain order parameters given as [29]:

$$K_i = \frac{1}{3} + \frac{\beta_i \Delta\alpha E^2}{k_B T}, \tag{2.3}$$

where $i \in \{x, y, z\}$ denotes a Cartesian dimension in the laboratory frame, $\beta_i \in [0, 1]$ is a coefficient dependent on the geometry and $\Delta\alpha$ is the difference in molecular polarisation between the axis of the light polarisation and the axis which is perpendicular to both the axis of light polarisation and the wave vector. Taking glycine parameters as an example, $\Delta\alpha = 2 \cdot 10^{-40}$ F m and a commonly used NPLIN laser intensity of $E = 3 \cdot 10^7$ V m^{-1} [9] it is found that $\Delta\alpha E^2 = 2 \cdot 10^{-5} k_B T$. Consequently, molecular orientations of glycine should marginally deviate from the unexposed orientations. Moreover, Knott *et al.* [30] have shown through Monte Carlo simulations that the energy contributions are unlikely to have any effect on the crystallisation rates. Therefore, it is unlikely that OKE is the sole mechanism for explaining NPLIN phenomena.

Notably, the OKE will not play any role for the simulations in this paper because the K^+ and Cl^- ions are not anisotropically polarised.

2.3.2. Dielectric polarisation

The electric field component can interact with molecules regardless of any static polarisation through dielectric polarisation (DP). According to DP, the oscillating electric field induces a transient polarisation in the molecules. In particular, the electric field adjusts the relative stability of the crystalline arrangement because its dielectric permittivity ε_p differs from the dielectric permittivity of the solution ε_s. Alexander and Camp [9] have derived an expression of the nucleation probability p as a function of I. In presence of a laser beam of intensity I, ΔG becomes

$$\Delta G = A\sigma + V\left(\rho\Delta\mu - \varepsilon^* I\right), \tag{2.4}$$

where ε^* is an effective permittivity given as

$$\varepsilon^* = \frac{3\varepsilon_s(\varepsilon_p - \varepsilon_s)}{c(\varepsilon_p + 2\varepsilon_s)}, \tag{2.5}$$

where $c = 1/\sqrt{\mu\varepsilon}$ is the speed of light in the medium of magnetic permeability μ and dielectric permittivity ε. Therefore, the electric field adds an a driving term to the nucleation. The expression for the nucleation probability based on I and a lability coefficient now becomes [9]:

$$p_{\text{nucleation}} = 1 - e^{-mI}. \tag{2.6}$$

Under the postulate that the I can be replaced with an effective intensity, $I_{\text{eff}} = I - I_{\text{thresh}}$, the expression in Equation 2.6 accurately predicts the nucleation probability for a variety of alkali halides, as seen in Figure 2.1.

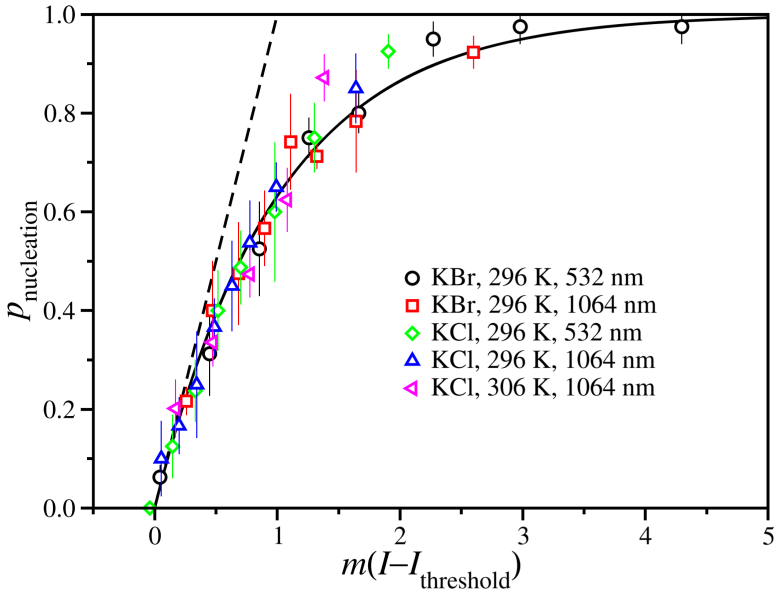

Figure 2.1: The probability of nucleation plotted against the product of the lability coefficient m and the intensity above the nucleation threshold intensity $I - I_{\text{thresh}}$ for different wavelengths and alkali halides at $S(296\text{K}) = 1.06$. Image taken from Alexander & Camp [9].

The derivation leading to Equation 2.6 is based on the assumption that the nucleation in a collection of vials follows a Poisson distribution with N_{cryst} the number of viable crystals over all the samples, such that $p_0 = e^{-N_{\text{cryst}}}$ is the probability that no crystals are observed. Notably, σ is the only fitted parameter for any alkali halide in Figure 2.1, which its still within an interval of wide range of values found in the literature [31].

In some NPLIN experiments, the nucleation is induced using a pulsed laser rather than a continuous laser beam [8]. If it is assumed that the DP clustering should occur during the laser pulse, a minimum pulse duration Δt_{min} may be derived. Subsequently, Δt_{min} may be compared to pulse durations employed in experiments. If the experimental duration is shorter, there is insufficient time for a crystal to form during the pulse. A minimum pulse duration of $\Delta t_p = 10^2$ ps has been derived for KCl crystals [2]. However, the derivation of this pulse duration is only valid for a homogeneous distribution of solutes before exposure. Although such a distribution is predicted by CNT, many other nucleation theories rely on a distribution of subcritical clusters before exposure [32]. Consequently, only experimental results with pulse durations longer than Δt_p can be explained using DP under the assumption of CNT, despite the strong quantitative agreement seen in Figure 2.1.

Notably, DP will not be relevant for the simulations in this paper because the K^+ and Cl^- ions are modelled as static point charges, so that that no transient polarisation can be induced.

2.3.3. Cavity-induced pressure-enhanced nucleation

As pressure differences are a known means of inducing nucleation, e.g. in sonocrystallisation [33], some ways in which pressure differences may lead to crystallisation will be discussed here. Kacker *et al.* [34] have reported that no difference in nucleation rates is observed between unexposed vials and vials masked with black tape, making it unlikely that the rates are increased by pressure waves emanating from the container. Therefore, nucleation due to electromagnetic absorption can only occur if the energy is absorbed by the solution. As the uptake of electromagnetic energy is approximately proportional to the exposed area, the largest localised amounts of energy should be absorbed by nanoparticles. As substantial heating of these particles

may lead to the formation of cavitation bubbles, the largest changes in concentration and pressure will probably occur in the vicinity of these nanoparticles.

The *cavitation cycle* and its suggested pressure-related effects will be discussed here, whereas the next subsection will contain a discussion of concentration-related consequences of the cavitation cycle. The process is displayed in Figure 2.2 in steps a) to e). a) An impurity or nanoparticle in an electrolyte solution is exposed to a laser beam and rapidly heats up through absorption of energy. b) The elevated temperatures lead to rapid evaporation of the surrounding solution within an evaporative layer. As a consequence, a shockwave originates from an expanding cavitation bubble. c) At some point, the cavitation bubble reaches its maximum size and its size is temporarily stationary. d) The cavitation bubble starts to collapse under the pressure of the surrounding fluid e) Another shockwave is generated upon collapse of the cavitation bubble. Although the clusters are shown at a particular location in the last frame for visualisation, it is currently unknown where and when these crystals are formed in relation to the process. If sufficient energy has been added to the system, the cavitation cycle may repeat itself in so-called *rebounds* [13]. Cavitation cycles can be generated on a variety of time and length scales, depending on the energy added to the system [13, 35].

If crystallisation occurs due to these shockwaves formed at heated nanoparticles, the process can be described as cavity-induced pressure-enhanced nucleation (CIPEN) [2]. In order to ensure that the effect occurs at intensities within the experimental range of NPLIN, relevant energies have been calculated by van Waas [2] based on experimental data of shockwave induction. There, it is found that a laser intensity of $I = 1.3$ TW/(cm)^2 yields changes to $\Delta\mu$ of $O(0.1\ k_B T)$. In order words, in order to induce pressure changes which significantly adjust the driving term of nucleation, intensities of 3 orders of magnitude above the intensity order required for optical breakdown at $O(100$ MW/(cm)$^2)$. Therefore, CIPEN appears to be an unlikely mechanism for explaining phenomena pertaining to NPLIN, although it may still provide an explanation for certain PLIN phenomena.

If the nucleation is caused by the shockwaves, it may be conjectured that crystals will start appearing further away from the nanoparticle surface at coordinates related to the velocity of the shockwave V_{shock}.

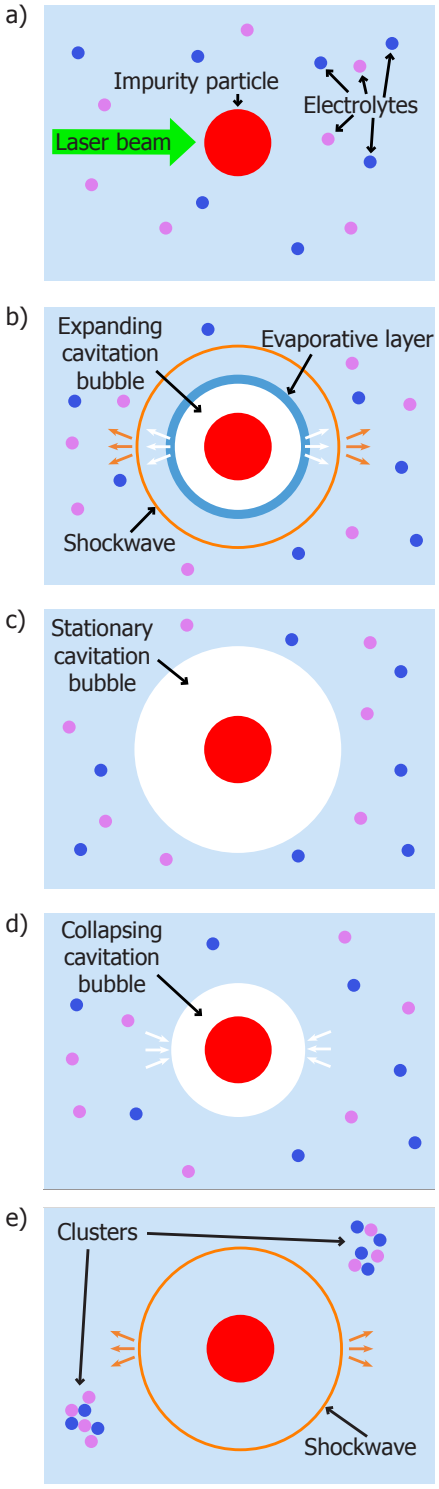

Figure 2.2: A schematic overview of the cavitation cycle in an electrolyte solution. The processes in the different steps are discussed in the text. Image obtained from [2].

2.3.4. Cavity-induced concentration-enhanced nucleation

In addition to causing pressure changes, the cavitation cycle may give rise to significant concentration changes. Nucleation due to concentration changes induced by the heated nanoparticle can be described as cavity-induced concentration-enhanced nucleation (CICEN) [2].

If the concentration rises above $S(T)$ in a region of sufficient size, crystals may start forming in the given region. As displayed in Figure 2.2, the solute particles in the evaporative layer will have to move into a new region upon evaporation of the solvent. If the evaporation occurs very rapidly, the solute particles will have no time to move into the surrounding fluid layers, effectively trapping them in the vapour bubble and giving rise to spontaneous crystallisation. If the evaporation occurs more gradually, the solute particles will migrate into the surrounding solution, which locally increases the concentration. It will be of interest for the simulations in this paper to verify the correlation between the longitudinal coordinates of any supercritical clusters and the longitudinal coordinate of the evaporative layer, if such an interface is well-defined in the given simulations.

If the solute particles are displaced into the surrounding solution, the nucleation may be related to temperature and concentration changes found outside of the cavitation bubble. Consider a region at a particular displacement from the nanoparticle surface with a concentration in the metastable zone for the initial temperature. As the electrolytes in the evaporative layer move into the surrounding water layers, the concentration in the region will increase. In addition, the temperature in the region will increase through heat dissipation from the nanoparticle. If the thermal energy difference is reduced faster than the concentration difference somewhere after the pulse, it is possible that the concentration in the region becomes labile, thus leading to spontaneous nucleation. The pathway visualised in the phase diagram of the solute is displayed in Figure 2.3.

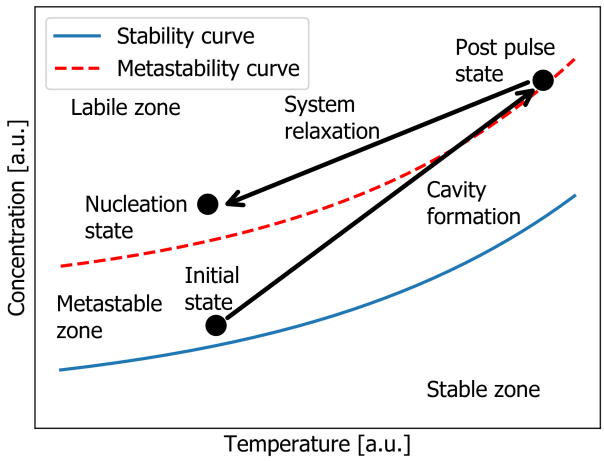

Figure 2.3: A potential pathway through the phase diagram in a region near the nanoparticle. The heated particle leads to increase of temperature and concentration in the region during and after the pulse. If thermal energy dissipates fast relative to the increased concentration, the region will end up in the labile zone, yielding for spontaneous nucleation. Image obtained from van Waas [2].

2.3.5. The continuum assumption

If the electrolyte particles move from the evaporative layer into the bulk solution and the electrolytes will still be distributed continuously at the short time scales and extreme conditions, then the concentration and temperature of the electrolytes may be modelled under the assumption that the system is a *continuum*, i.e. fluids can be described as a continuum, without regarding the fact that these fluids are composed of molecules. As the system contains a moving boundary condition, describing the concentration function using a partial differential equation is known as a Stefan problem [36]. Therefore, solving the problem with a continuum description may be provide useful results, as long as the assumption of a continuum and the behaviour of the solutes moving into the solution is valid. Such an approach has been developed to some extent by Soare [37]. In the same work, of Soare, crystals have been observed in solutions where laser-induced cavitation bubbles were formed. Contrasting the continuum approximation, it could not be determined whether these crystals resided inside of the cavitation bubbles, or on the bottom of the vials. If the electrolytes in the MD simulations behave in such a way that the continuum assumption is valid, it will allow for performing simulations at larger time and length scales using a continuum description.

2.4. Molecular dynamics

In sufficiently small and well-understood systems such as a in two-body problem, physical quantities can be evaluated through an analytical description or by considering all possible system states. In somewhat larger systems, statistical averages can be obtained provided that the system is ergodic and there are equal a priori probabilities [38]. In such systems, the statistical quantities can either be obtained by Monte Carlo simulations or by MD. In MD, the classical equations of motion of the particles in the system are numerically integrated in time, moving deterministically through a phase space [39]. Given an initialised collection of particles and a statistical ensemble, an MD algorithm can be used for deterministic time evolution of the system. MD is the integration method selected here for studying the NPLIN mechanisms because it can still be used for systems out of equilibrium, such as heated nanoparticles in solution.

The forces and relevant parameters which are accounted for in MD are determined by selecting so-called *force fields* [39]. First, relevant physical properties and their respective forces, such as the Lennard-Jones potential, Coulomb interaction and molecular vibrations, are selected. Subsequently, the accompanying equations are selected for these effects, such as the Coulomb equation or a quadratic potential for the molecular vibrations. Lastly, *force field parameters* are chosen for the force fields for the quantitative implementation of the physical properties. These parameters are generally based on experimental observations, theoretical models and validation through previous simulations [40].

2.4.1. Algorithms of molecular dynamics

The Velocity-Verlet algorithm is a time-reversible algorithm for performing time integration on atoms and molecules [39]. The derivation is based on Newton's equations of motion. The evaluation of position vectors $\boldsymbol{r}_i(t)$ of the respective i particles and velocity vectors $\boldsymbol{v}_i(t)$ over a time step Δt are found as:

$$\boldsymbol{r}_i(t+\Delta t) = \boldsymbol{r}_i(t) + \boldsymbol{v}_i(t)\Delta t + \frac{\boldsymbol{F}_i(t)\Delta t^2}{2m_i} \tag{2.7}$$

where $\boldsymbol{F}_i(t)$ is the force vector on particle i at time t and m_i is the mass of particle i. Once the displacements have been calculated at $t+\Delta t$, the new forces $\boldsymbol{F}_i(t+\Delta t)$ can be calculated. Subsequently, $\boldsymbol{v}_i(t+\Delta t)$ is calculated using

$$\boldsymbol{v}_i(t+\Delta t) = \boldsymbol{v}_i(t) + \frac{\boldsymbol{F}_i(t) + \boldsymbol{F}_i(t+\Delta t)}{2m_i}\Delta t \tag{2.8}$$

which completes the time integration step. Commonly, the system is initialised by generating random particle positions and velocities according to an assumed distribution [20]. Lastly, physical properties and averages, such as the T and the density ρ can be calculated for the given step. As the Velocity-Verlet algorithm takes into account terms up to $O((\Delta t)^2)$ and third order terms are cancelled out against each other during the derivation, the minimum Velocity-Verlet errors are of $O((\Delta t)^2)$ [39], although long time errors can arise of $O((\Delta t)^4)$ [41]. In any ensembles where the temperature was kept constant, a Nosé-Hoover thermostat was applied. According to this thermostat, the displacement derivative $\dot{\boldsymbol{r}}_i$ and total momentum derivative $\dot{\boldsymbol{p}}_i$ of particle i are found using the Nosé-Hoover equations [42]:

$$\dot{\boldsymbol{r}}_i = \boldsymbol{v}_i = \frac{\boldsymbol{p}_i}{m_i} \tag{2.9}$$

$$\dot{\boldsymbol{p}}_i = \boldsymbol{F}_i - \dot{\eta}\boldsymbol{p}_i \tag{2.10}$$

$$\dot{\eta} = \frac{p_\eta}{Q} \tag{2.11}$$

$$\dot{p_\eta} = \sum_i^N \left(\frac{\boldsymbol{p}_i \cdot \boldsymbol{p}_i}{m_i}\right) - g k_B T_p \tag{2.12}$$

here, T_p is the prescribed temperature, g is the number of degrees of freedom, $Q \propto g k_B T/\omega$ is a coupling mass term and $\dot{\eta}$ may be regarded as a dynamic friction coefficient and N is the number of particles. The magnitude Q relates to the so-called *thermostatting frequency* ω, determining how strongly the thermostatting occurs in time [43]. The momenta are scaled during the integration steps such that the temperature changes towards T_p.

2.5. Geometric effects

In this section, two consequences of the selected modelling geometry will be discussed. Although the subjects are theoretical and should therefore be treated in the current chapter, the relevance should only become clear upon reading Section 3.2.

2.5.1. Interfacial tension

As can be seen from Equation 1.1, ΔG will depend on the shape of the crystal being formed. Notably, for a crystal shaped as a rectangular cuboid with square facial area a and width w in a box which is periodic along the faces parallel to w, Equation 1.1 yields

$$\Delta G = a\left(2\sigma + w\rho\Delta\mu\right), \tag{2.13}$$

where the surface tension in the periodic dimensions vanishes and the factor of 2 arises from the surfaces on the four non-periodic faces. Such a crystal may be anticipated as it results in crystals having very small surface tension area and thus being formed favourably. Notably, ΔG now scales linearly with a such that the crystallisation rate should exponentially depend on the surface area of the non-periodic dimension. Moreover, the relation between the surface tension and the curvature of the interface area can be expressed as an expansion in $1/r$, where r is the radius of the crystal:

$$\sigma(r) = \sigma_0\left(1 - \frac{2\delta}{r} + O(\frac{1}{r^2})\right), \tag{2.14}$$

[44] where σ_0 is the interface tension of a crystal of infinite radius and δ is known as the *Tolman length*. δ is a parameter which accounts for the change in interfacial tension with r. Peculiarly, $\sigma = \sigma_0$ for a planar rectangular cuboid crystal as r goes to infinity for a plane. Additionally, the influence of the curvature can be estimated up to first order in $1/r$. Since no estimates of δ could be found for KCl, the comparison will be performed for NaCl, which is an alkali halide having chemical properties similar to KCl.

For NaCl, a Tolman radius of $\delta = 0.13$ nm has been reported for an NaCl crystal-solution interface [45]. Combining this with a interfacial tension of $\lambda = 81.75$ mJ/m^2 [46] at supersaturation for NaCL, λ_0 can be found by assuming that at saturation, any forming crystals will initially have $r = r_c$, where it is reported that $r_c = 1.095$ nm for NaCl [47]. Consequently,

$$\sigma_0 = \frac{\sigma(r_c)}{1 - \frac{2\delta}{r_c} + O(1/r_c^2)}. \tag{2.15}$$

Neglecting the higher order terms, the given parameters yield $\sigma_0 = 107.2$ mJ/m^2. Clearly, the interfacial tension of plane is higher than that of a curved surface and obtaining a perfect plane leads to a surface tension increase of 31% compared to a surface at the critical radius. Furthermore, it is conjectured that the interfaces of formed crystals on the column will have outwards curvature, as this leads to a lower σ.

2.5.2. Geometry and heat dissipation

One of the consequences of taking a rectangular cuboid system rather than a conically shaped system is that the thermal energy in the system will dissipate at a lower rate. The reaction system studied in this paper is considered to be a closed thermodynamic system, whereas it will be an open system in practice. Moreover, the thermal energy of a sphere in 3 dimensions which is thermostatted along its outer radius will dissipate faster than the thermal energy of a column which is thermostatted at a single plane.

To obtain an estimate of the effect of geometry on dissipation of thermal energy, the spherical and 1D longitudinal temperature distributions will be considered. The following representations of the 1D and 3D systems have been chosen such that the mathematical solutions are well-known, while a comparison between the modelled 1D longitudinal and physical 3D spherical system is still meaningful.

It is assumed that the system consists of water vapour at an initial temperature of $T_\mathrm{i} = 373$ K. The temperature on one of the boundaries is then instantaneously raised to a temperature of $T_\mathrm{f} = 837$ K and kept at this temperature for $t > 0$. With these temperatures, no phase transitions for the water vapour will occur. This boundary is is represented as the left surface for the 1D system and as a sphere of nonzero size a at the centre of the 3D spherical system. The other boundary condition is that $T \to T_\mathrm{i}$ as $r \to \infty$. If the thermal energy can only redistribute itself through diffusion, the temperature distribution can be described by the heat equation [48]:

$$c_P \rho \frac{\partial T}{\partial t} = \frac{\partial}{\partial x}\left(K_0 \frac{T}{x}\right) + Q(x,t), \tag{2.16}$$

Where c_P is the heat capacity at constant P, ρ is the density of the solution and K_0 is the thermal conductivity. Moreover, $D = K_0/(c\rho)$ is known as the thermal conductivity. Here, $Q(x,t)$ represents a source of thermal energy. For the system of study, potential energy may turn into thermal energy during the formation of crystals, leading to $Q(x,t) \neq 0$. Nonetheless, it will be assumed that $Q(x,t) = 0$ for the current derivation. If there is a sudden raise of temperature to T_f to the left hand boundary, the solution is found as [48]:

$$T(x,t) = T_\mathrm{i} + (T_\mathrm{f} - T_\mathrm{i})\,\mathrm{erf}\left(\frac{x}{\sqrt{4Dt}}\right), \tag{2.17}$$

where $\mathrm{erf}(z)$ denotes the error function, defined as [49]:

$$\mathrm{erf}(z) = \frac{2}{\sqrt{\pi}} \int_0^z e^{-\eta^2} \mathrm{d}\eta. \tag{2.18}$$

In 3D, the spherically symmetric heat equation in absence of any thermal energy source $Q(r,t)$ becomes [48]

$$\rho c_p \frac{\partial T}{\partial t} = \frac{1}{r^2}\frac{\partial}{\partial r}\left(K_0 r^2 \frac{\partial T}{\partial r}\right), \tag{2.19}$$

and the solution becomes:

$$T(r > a, t) = T_\mathrm{i} + (T_\mathrm{f} - T_\mathrm{i})\left(\frac{a}{r}\right)\mathrm{erf}\left(\frac{r-a}{\sqrt{4Dt}}\right), \tag{2.20}$$

in addition to the imposed $T(r \leq a, t) = T_R$ inside the spherical particle. In order to compare temperature distributions from equations 2.17 and 2.20, an average value of $D = 1.32 \cdot 10^{-7}$ m^2/s at $T = 623$ K for water vapour is taken [50].

The solutions according to both equations are found in Figure 2.4 for $0 \leq x \leq 500$ Å and $0 \leq r - a \leq 500$ Å.

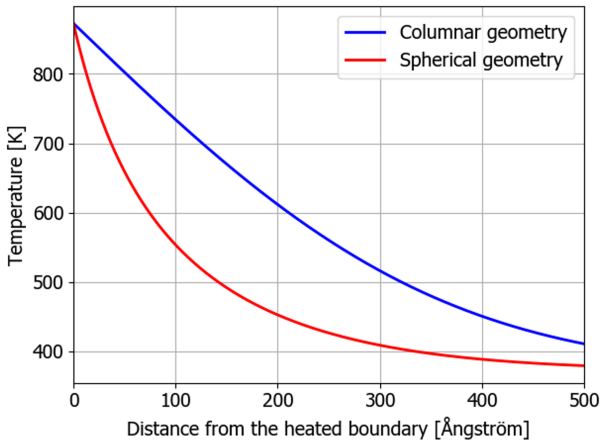

Figure 2.4: Temperature distributions for the columnar (1D) and spherical (3D) geometries. A column of water vapour at $T_\mathrm{i} = 373$ K is placed on top of a surface (1D) or a nanoparticle of radius $r = 10$ nm (3D). The boundaries are instantaneously raised to $T_\mathrm{f} = 873$ K and held at this temperature. The temperature distributions are found after $t = 3$ ns with a water vapour diffusivity of $D = 0.132 \cdot 10^{-7}$ m^2/s.

From Figure 2.4 it is concluded that there the non-equilibrium temperature distribution is very different for the two geometries. The difference will probably still be significant for the system used for MD simulations in this paper, despite the occurrence of K^+ and Cl^- ions and a moving liquid-vapour boundary.

3

Modelling methods

This chapter contains a description of the modelling methods which allow for performing meaningful MD simulations on the nanoparticle heating mechanisms. Particular software, the combination of which allows for performing MD simulations from system creation to post-processing, is mentioned in Section 3.1. The modelling of the MD system is described in Section 3.2. Additionally, the force fields and additional input parameters is described in Section 3.3. The intent of Section 3.3 is to provide sufficient detail for the simulations to be repeated. However, a complete description of all of the selected parameters and settings is considered outside of the scope of this report. Lastly, evaluation of physical quantities is described in Section 3.4.

3.1. Software, HPCs and builders

All simulations were performed using the Large-scale Atomic/Molecular Massively Parallel Simulator (LAMMPS) version June 5 2019 [51, 52]. LAMMPS is an open source classical molecular dynamics code and it is based on C++. All calculations were performed using HPC cluster 5 of Delft University of Technology.

Water molecules and electrolytes were constructed using Moltemplate [53]. Graphene atoms were positioned in Moltemplate and bonds were constructed in VMD. A Fe_2O_3 surface was constructed using the LAMMPS builder by Echeverri Restrepo and Ewen [54, 55], which is based on Moltemplate.

Post-processing and plotting of data was performed using Python [56] and graphical analysis was performed using Visual Molecular Dynamics (VMD) [1]. A visualisation of the system model was made using Adobe InDesign [57]. A video was constructed using Adobe Premiere Pro [58] and Adobe Media Encoder [59].

3.2. Modelling the system

First, the approximate size of the system was determined. Ideally, the system of study would be of the size of experimental vials. However, simulating a couple of hundreds of molecules for a time of the order of nanoseconds can readily require several thousands of CPU-hours [20]. Given the computational resources available for this study, it was decided to perform the simulation on a system containing approximately 20,000 atoms.

3.2.1. Composition of the system

The starting point for the creation of a model is the spherical nanoparticle in solution, as displayed in Figure 2.2. The model system for the MD simulations should sufficiently resemble the physical configuration, in order to obtain meaningful results. It was assumed that on average, the system variables such as temperature, density and electrolyte ordering should be distributed homogeneously along any axis perpendicular to the nanoparticle surface, i.e. the system exhibits spherical symmetry. Consequently, a conically shaped region with its central axis parallel to the normal of the nanoparticle surface was considered as an ideal geometry for the simulations. However, imposing periodic boundary conditions on a conically shaped region is far from trivial. Therefore, the system was modelled as a rectangular cuboid. The difference between a conically shaped region and such a water column is small when the column height is small compared to the size of the nanoparticle. Javid *et al.* [25] have reported a reduction of nucleation rates upon filtering solutions with a 200 nm pore size, suggesting that the larger nanoparticles can be of O(100 nm) in size. Therefore, it was assumed that the nanoparticle surface could be considered planar and that useful results could be obtained with simulations using a system shaped as a rectangular cuboid of length O(10 nm).

The nanoparticle surface was composed of Fe_2O_3 (hematite) to accurately reflect the behaviour of commonly found impurities. The Fe_2O_3 was positioned with its bottom surface at $z = 0$ for all simulations. Moreover, the Fe_2O_3 imposed discrete values of the width Δx and height Δy and the thickness of the iron oxide, as Fe_2O_3 structures could only be generated with an integer number of lattice vectors. As $a_x = a_y = 5.029$ Å, it was decided to use $\Delta x = \Delta y = 4a_x = 20.116$ Å. In addition, a Fe_2O_3 thickness of $a_z = 13.370$ Å was selected. Only the top layer of the Fe_2O_3 of thickness $\Delta z = 5.0$ Å was time integrated because sufficient amounts of thermal energy could be added to the system for the given thickness. A solution of K^+ and Cl^- ions was placed on top of the α-$Fe_2O_3(0001)$ surface. The solution was composed of water molecules and K^+ and Cl^- ions in equal amounts such that $S(298\,\mathrm{K}) = 1.05$ as a typical experimental supersaturation, corresponding to a concentration of $c = 0.373$ g KCl / (g H_2O). At $T = 298$ K, the total column had an equilibrium length of $\Delta z_0 = 486$ Å. The bonds lengths and LJ equilibrium lengths of the graphene were adjusted from $r = 1.42$ Å to $r_0 = 1.45175$ Å in order fit an integer number of carbon atoms into the system and σ_C was scaled by the same ratio. Moreover, the x and y coordinates of the carbon atoms were fixed, so that the graphene layer would operate as a planar piston. In addition, the graphene layer was thermostatted during at $T = 298$ K during all simulations to allow for dissipation of thermal energy required for completion of the cavitation cycle. The final system is displayed in Figure 3.1.

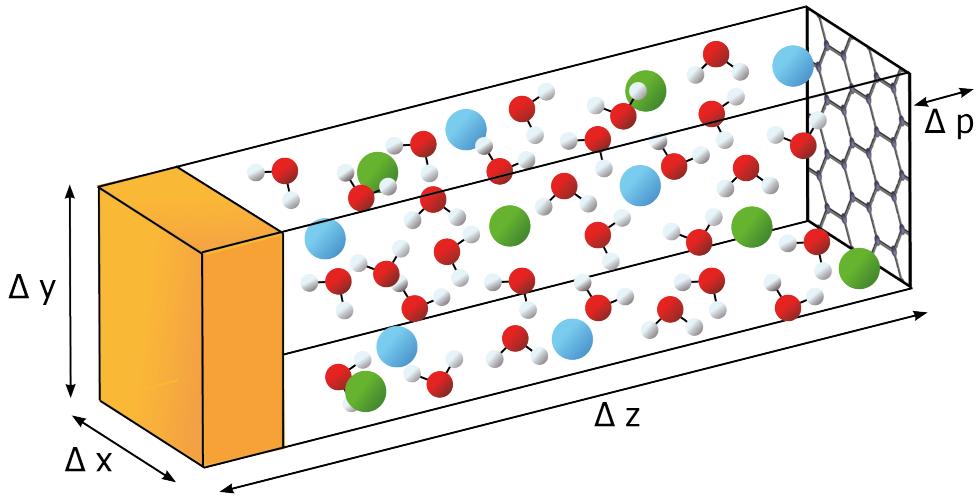

Figure 3.1: The model of the system which will be used in the MD simulations. K^+ (blue) and Cl^- in an aqueous solution are enclosed between a stationary Fe_2O_3 surface on the left hand side and a graphene-like sheet on the right hand side. All atom types are coloured according to the CPK colouring [60], except for K^+ ions in blue and the Fe_2O_3 block in orange. The dimensions are denoted as Δx for the width, Δy for the height and Δz for the length. ΔP is the pressure exerted on the graphene.

In order to decrease undesired long range Coulomb interactions through the periodic z direction, the column height was equilibrated for a variety of total system lengths. As a consequence, it was decided to maintain a minimum of 200 Å empty space between the graphene sheet and the periodic boundary, as the equilibrium column length differed by less than 0.1 Å between the equilibrium length with 1000 Å of empty space.

As the expressions for ΔG in Chapter 1 are valid for ensembles for equilibrium NPT ensembles, the pressure in the system by applying an external force on the graphene sheet such that the pressure $\Delta P = F/A$ amounts to a constant temperature, where A is the area of the graphene sheet. Moreover, determining ΔG outside of equilibrium is valid provided that N (or μ), P and T are approximately constant for a given region. Thus, it will be possible to evaluate the stability of clusters using Equation 2.13 provided that the an NPT ensemble is locally applicable [38].

3.2.2. Simulated systems

The following simulations will be considered. First, the system will be equilibrated in a time of $\Delta t = 1$ ns. Next, the system will be heated in a time of $\Delta t = 100$ ps as part of a total bubble expansion time of $\Delta t = 1$ ns. Afterwards, the expanded system will be used as the input for two different system evolutions, which will be

induced by applying different ensembles. In the first case, the system is allowed to evolve adiabatically for another $\Delta t = 1$ ns of simulation time. In the second system, part of the solution will be thermostatted during a simulation time of another $\Delta t = 4$ ns, to ensure completion of the cavitation cycle.

During the simulations, parts of the system were integrated using various integration ensembles. In the NVE ensemble, the particle total momenta are directly obtained from the Velocity-Verlet algorithm. In the NVT ensemble, the particle momenta are modified using the Nosé-Hoover equations.

3.2.3. Temperature estimation of the heated nanoparticle

In this subsection, an estimate of the nanoparticle temperature after exposure is obtained. Assuming a spherical nanoparticle of radius R with a mean heat capacity per unit volume of $c_p/V = 3.41 \cdot 10^6$ J m^{-3} K^{-1} in the interval of $T \in [298, 1500]$ K, the temperature increase ΔT can be found from an energy balance:

$$\Delta T = \frac{\Delta E}{c_p} = \frac{3\pi R^2 I \Delta t}{4\pi R^3} \frac{V}{c_p} = \frac{3 I \Delta t}{4R} \frac{V}{c_p} \tag{3.1}$$

Taking typical experimental parameters of $I = 10$ MW/(cm)^2, $\Delta t = 6$ ns [34], and assuming that $R = 0.1$ µm, it is found that $\Delta T = 1320$ K. Therefore, an initial temperature of $T_\mathrm{i} = 298$ K will be raised to roughly $T_\mathrm{f} = 1500$ K, which will be taken as the raised nanoparticle temperature for the simulations. Notably, a particle threshold temperature for the observation of vapour expansion in MD simulations is reported by Sasikumar and Keblinski [61], where $T_\mathrm{thresh} = 1050$ K for a particle radius of $R = 4$ nm is provided as an example. However, larger raised temperatures of thousands of Kelvin are required for a well-defined vapour-liquid interface. Here, it will be attempted to generate a vapour phase with the lifetime of several ns and the size of several tens of nm.

3.3. Force fields

The system was modelled by considering Lennard-Jones (LJ) interactions between particles whose distance was within a cutoff radius of $r_\mathrm{LJ} = 10$ Å and to consider Coulomb interactions between particles at any distance, describing the solution as a LJ-fluid. Long range Coulomb interactions were evaluated using the *particle-particle-particle-mesh* (pppm) k-space style. The pppm is a fast long range interaction solver [62]. However, it does impose that periodic boundaries can only be used for all of the system boundaries, or not at all.

Most of the parameters in this paper are related to the ClayFF force field [63]. The functional form of the energy of the ClayFf force field is given as:

$$E_\mathrm{total} = E_\mathrm{Coulomb} + E_\mathrm{vdW} + E_\mathrm{bond\text{-}stretch} + E_\mathrm{angle\text{-}bend}, \tag{3.2}$$

where angle bend energies will not be taken into account in this paper. Lastly,

$$E_\mathrm{Coulomb} = \frac{e^2}{4\pi\varepsilon_0} \sum_{i \neq j} \frac{q_i q_j}{r_{ij}} \tag{3.3}$$

$$E_\mathrm{vdW} = \sum_{i \neq j} 4\varepsilon_{ij} \left[\left(\frac{\sigma_{ij}}{r_{ij}} \right)^{12} - \left(\frac{\sigma_{ij}}{r_{ij}} \right)^{6} \right] \tag{3.4}$$

$$E_\mathrm{bond\text{-}stretch} = \sum_{\mathrm{bonds}} k_{ij} \left(r_{ij} - r_0 \right)^2 \tag{3.5}$$

where ε_0 is the dielectric permittivity of vacuum, $r_i j$ is the distance between particles i and j and k_{ij} is the bond stretch parameter.

The K^+, Cl^- and H_2O parameters were taken from Cygan *et al.* [63] as included in the ClayFF force field. The ClayFF force field is a general force field for potentially hydrated mineral systems and their interactions with aqueous solutions [63] whereas its description of water is based on the SPC model. The Fe_2O_3 parameters were taken from Berro *et al.* for the [64] charges and Savio *et al.* [65] for the LJ-parameters according to the L-OPLS force field. The molecular geometry was constructed based on the description of hematite by Blake *et al.* [66]. Modified LJ-parameters for the carbon-water interactions were taken from Werder *et al.* [67].

The LJ-parameters $\varepsilon_{i,j}$ and $\sigma_{i,j}$ between particles of different species i and j were, unless specified otherwise, calculated using the Lorentz-Berthelot mixing rules [68]:

$$\varepsilon_{i,j} = \sqrt{\varepsilon_i \varepsilon_j}$$
$$\sigma_{i,j} = \frac{\sigma_i + \sigma_j}{2}. \tag{3.6}$$

The species and their respective charges, LJ-parameters and bond coeffients are found in Table 3.1.

Table 3.1: Overview of the different parameters used in the simulation of this paper. Ox denotes oxygen found in Fe_{2O3}, whereas O denotes oxygen found in H_2O. Here, r_c = 10 Å denotes the cutoff for LJ-interactions.

Species	**q/e [-]**	**σ [Å]**	**ε[kcal/mol]**	**Source**
K^+	1.0	3.3340	0.1000	[63]
Cl^-	-1.0	4.4000	0.1001	[63]
H	0.4238	2.058	0.0000	[69]
O	-0.8476	3.1655	0.1554	[69]
Fe	0.7170	2.3200	0.3400	[64, 65]
Ox	-0.5140	2.9600	0.1700	[64, 65]
C	0	3.483	0.068443	[70]
Species i	**Species j**	**$\sigma_{i,j}$ [Å]**	**$\varepsilon_{i,j}$[kcal/mol]**	**Source**
C	O	3.2800	0.11400	[67]
C	H	3.2800	0.0000	[67]
Bond	**r_0** [Å]	**k [kcal/(mol Å ^{2})]**	**Range**	**Source**
Fe−Ox	1.945	130.0000	1.9-2.0	[64, 66]
Fe−Ox	2.116	130.0000	2.0-2.5	[64, 66]
Ox−Ox	2.888	130.0000	2.8-2.9	[64, 66]
Ox−Ox	2.775	130.0000	2.7-2.8	[64, 66]
Ox−Ox	2.669	130.0000	2.6-2.7	[64, 66]
Fe−Fe	2.971	130.0000	2.9-3.0	[64, 66]
O−H	1.0000	554.135	0-r_c	[63]
C−H	1.451897	500.0000	0-r_c	[71]

3.4. Post-processing of data

The temperature and number of bonded ions were calculated during post-processing using the output of particle displacements and velocities at several time steps.

3.4.1. Temperature calculations

As obtaining the temperature of a statistical ensemble depends on the degrees of freedom of the system, it will be discussed here how the temperatures of the system will be obtained using post-processing. The instantaneous velocities of Equation 2.8 are used to calculate the temperature of the water molecules in the column.

According to the equipartition theorem, each quadratic degree of freedom contributes $k_B T/2$ to the total internal energy of a molecule [72]. During the simulations, vibrational degrees of freedom were disregarded. Consequently, the temperature of the water molecules could be calculated using 3 out of its 6 degrees of freedom as

$$T = \frac{\langle E_{kin} \rangle + \langle E_{rot} \rangle}{3Nk_B} = \frac{2\langle E_{kin} \rangle}{3Nk_B} = \frac{1}{3Nk_B} \sum_{i=1}^{N} m_i \boldsymbol{v}_i \boldsymbol{v}_i = \frac{1}{3Nk_B} \sum_{i=1}^{N} \sum_{j=1}^{3} m_i v_{i,j} \cdot v_{i,j} \tag{3.7}$$

where $v_{i,j}$ denotes the velocity of particle i in the jth Cartesian dimension. Temperatures were time averaged at over n frames by considering velocities ranging from the data at time instant $k-(n-1)/2$ up until the time instant of $k+(n-1)/2$ in other reduce the influence of finite size effects.

3.4.2. Supercritical Cluster Evaluation

In order to quantify the extent of clustering, two properties will be calculated for the simulation results, in addition to visual inspection. First, the number of ions satisfying a bond order criterion will be evaluated at

different time steps. Here, an ion is considered clustered according to the bond order criterion provided by Sindt *et al.* [15] if it has 5 or more neighbouring ions within a displacement of $r = 3.6$ Å as the first minimum in the radial distribution function (RDF) of KCl [73]. Second, equations 2.2 and 2.13 can be combined to obtain an estimate for the minimum width w_{min} for thermodynamically stable configurations having $\Delta G < 0$. Such stable configurations are found when

$$w_{\text{min}} > \frac{2\sigma}{\rho k_B T \ln(S)}. \tag{3.8}$$

It will be assumed that $\sigma_0 = 1.31 \cdot \sigma$ for KCl analogous to the relation for KCl, such that a value of σ_0 for planar KCl-water interfaces is available. Taking $\rho = 2.603 \cdot 10^{28}$ m^{-3} and $\sigma = 78.58$ mJ/m^2 [9], $\sigma_0 = 1.31 \cdot \sigma$, $S(298\,\text{K}) = 1.05$ and $T = 298$ K, it is found that $w_{\text{min}} = 2.6$ nm as the minimum width of critical clusters. As crystals not having the shape of a rectangular cuboid will have a larger surface-to-volume ratio, a larger size of these crystals is required for these crystals to be stable. Using σ for the surface tension, combining equations 2.2 and 1.3 yields a minimum radius of $r_c \geq 1.47$ nm.

Although the observation of crystallisation in MD would require metadynamics, the general argument is that clusters satisfying $\Delta G < 0$ are equivalent to obtaining nucleation in macroscopic physical systems. Therefore, if such clusters are found in regions where an NPT ensemble applies locally, it will be argued that nanoparticle heated crystallisation is feasible.

4

Results & discussion

In this chapter, the results of the simulations are discussed. Physical quantities for the equilibrium system are provided in Section 4.1. The equilibrium system is discussed in Section 4.1. The results of a nanoparticle heating simulation of time interval $\Delta t = 1$ ns, leading to an intermediate system, are provided in Section 4.2. The results of an adiabatic evolution of this intermediate system from $t = 1$ ns to $t = 2$ ns are found in Section 4.3. Section 4.4 contains the results of cooling the intermediate system from $t = 1$ ns to $t = 5$ ns, completing the cavitation cycle. A video showing the system evolution discussed in sections 4.2 and 4.4 in sequence is provided at `http://tinyurl.com/nanoparticleheating`. The consequences of using a columnar system geometry are discussed in Section 4.5. Lastly, the CICEN and CIPEN mechanisms are evaluated in Section 4.6.

A time step of $dt = 1$ fs was used in all simulations. All histogram bins in this chapter were generated at equal width. In order to reduce finite size effects, all physical properties were calculated by averaging over 3 frames with $\Delta t = 1$ ps between each frame.

4.1. Equilibrium system

First, the system was initiated by assigning velocities to the water molecules and the K^+ and Cl^- ions according to a Gaussian distribution such that the mean system temperature would be $T = 298$ K. Afterwards, a thermostat was applied to the system at $T = 298$ K and applying a pressure of $P = 1$ atm on the piston for a time integration for $\Delta t = 1$ ns. In addition, the number of clustered ions was calculated given the criteria described in 3.4.2. The temperature profile, density profile, clustered ions and the system are displayed in Figure 4.1.

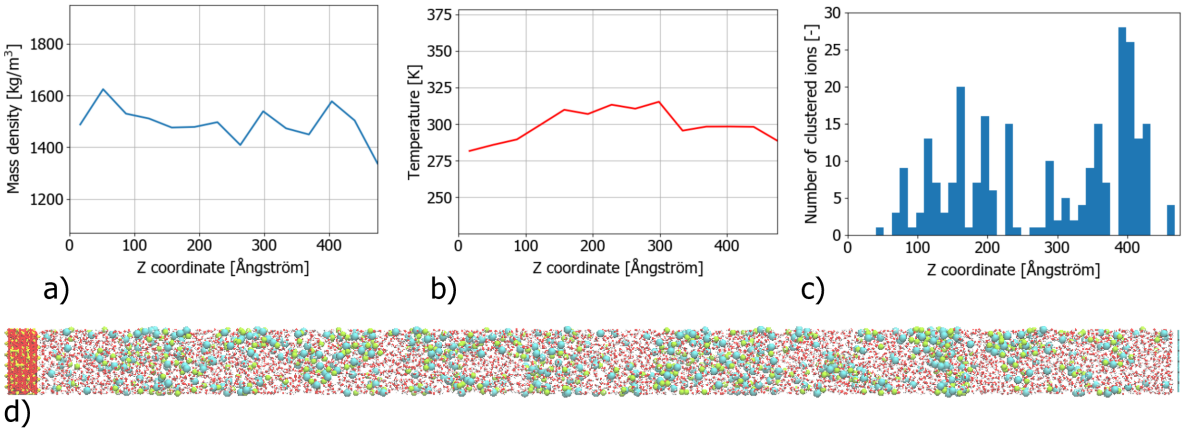

Figure 4.1: a) The density of the solution, b) the temperature of the solution, c) distribution of clustered ions and d) the system in equilibrium at t = 0. In the system, the Fe_2O_3 surface is found on the left, the K^+ (blue) and Cl^- (green) ions are distributed in the water in the middle and the system is enclosed by the graphene piston on the right.

As can be seen in Figure 4.1, there is some fluctuation of the density and temperature along the z coordinate. Average profiles for these quantities could be obtained by averaging over longer time scales. However, longer

equilibration times did not lead to a visible reduction in the fluctuations of the temperature along the z-coordinate. In addition, some of the clusters already satisfy the bond order criterion, similar to what is seen in the simulations by Sindt *et al.* [15] before any heating.

Notably, the average density is significantly larger than the experimental density of saturated solutions of $\rho = 1180$ kg/m^3 at $T = 298$ K [74]. It is suggested that the majority of the deviation in the density is due to incorrect input of one or more parameters into LAMMPS. Part of the density difference may be attributable to the inability of the force field to capture the complexity of the real physical system.

No cuboid crystals were observed during the $\Delta t = 1$ ns equilibration time. Moreover, no stable ion structures of O(nm) were observed. Therefore, it is unlikely that spontaneous nucleation should occur in the unperturbed system, in agreement with the notion that macroscopic KCl solutions are metastable at $S(298\,\text{K}) = 1.05$.

4.2. Cavitation bubble expansion phase

The nanoparticle was heated to $T = 1500$ K. The heating was performed in the first $\Delta t = 100$ ps of the simulation, similar to picosecond pulse NPLIN experiments [75]. Afterwards, the system expanded adiabatically until a total time of $t = 1$ ns. A pressure of $P = 1$ atm was maintained to allow fluid to expand during the interval. The results for the cavitation bubble expansion phase are displayed in Figure 4.2.

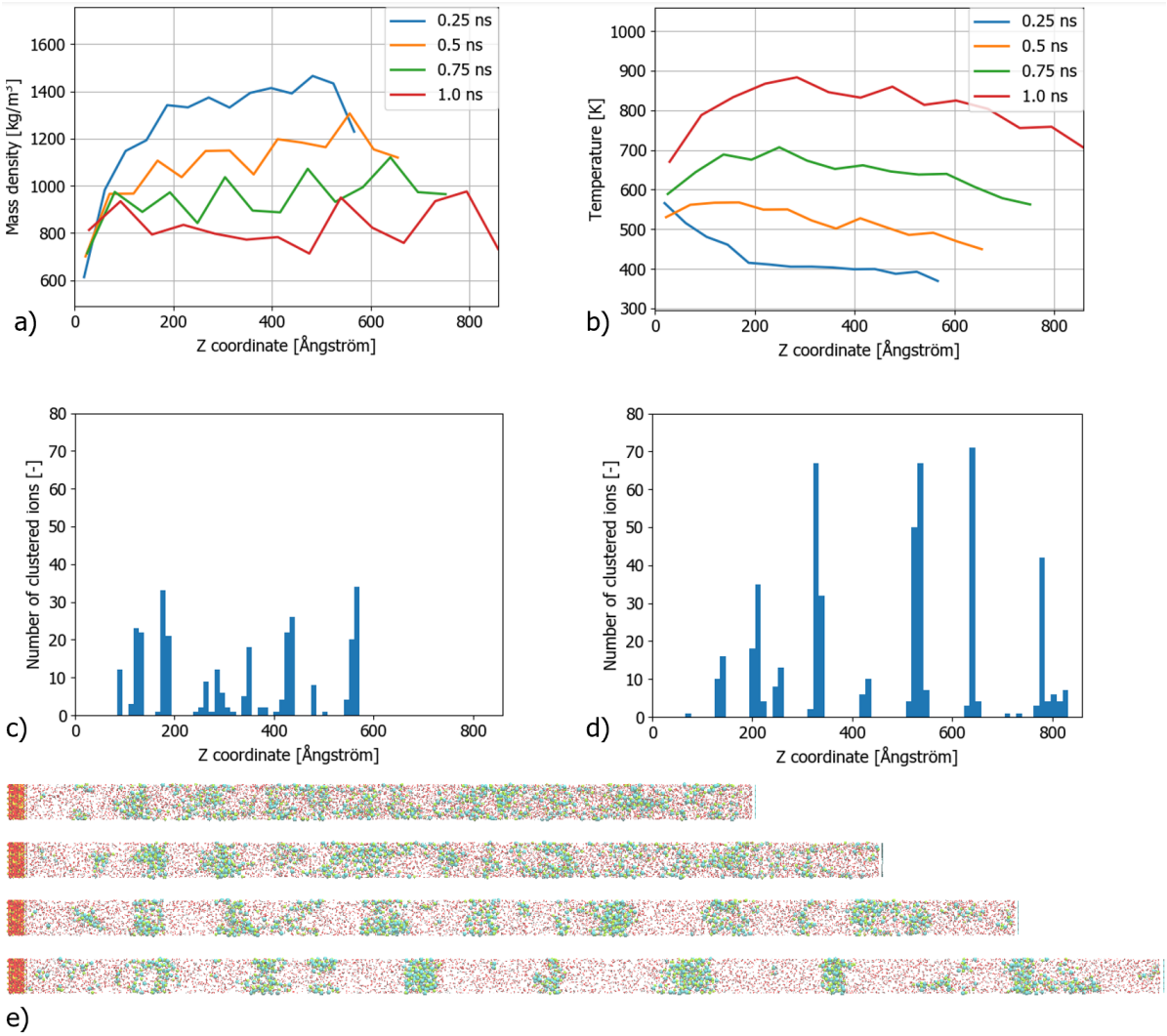

Figure 4.2: a) The density profiles at 4 instants, b) the temperature distributions at 4 instants, c) the number of clustered ions at $t = 0.5$ ns, d) the number of clustered ions at $t = 1$ ns and e) the system at $t = 0.25$ ns, $t = 0.5$ ns, $t = 0.75$ ns and $t = 0.1$ ns, respectively. The width of the bins is kept constant over the change in system size.

As can be seen from Figure 4.2, the system expands from its equilibrium length $\Delta z_0 = 486$ Å up to $\Delta z = 864$ Å. It can be seen that cuboid crystals start appearing at multiple locations in the column. The number of clustered ions per bin increases by almost an order of magnitude from the equilibrium system to the heated system. In the vapour segments at $t = 1$ ns, $\rho \approx 800$ kg/m^3, suggesting that P has become more or less constant over the system. Moreover, the temperature gradient $\Delta T/\Delta z$ is relatively small. Consequently, it may be argued that an NPT ensemble is applicable locally. Therefore, it is argued that the clustering observed in the model system corresponds to crystallisation in a physical system. Equivalently, the nanoparticle heating is considered as a plausible mechanism for nucleation.

4.3. Cavitation bubble stationary phase

In order to obtain a temporarily stationary cavitation bubble, $P = 4$ atm was applied to the graphene layer of the intermediate system. Such pressures are readily observed in MD simulations of cavitation bubbles [61] and should lead to completion of the cavitation cycle provided no additional energy is added to the system after initiation of the cycle. The results of continuing the simulation from $t = 1$ ns to $t = 2$ ns are shown in Figure 4.3.

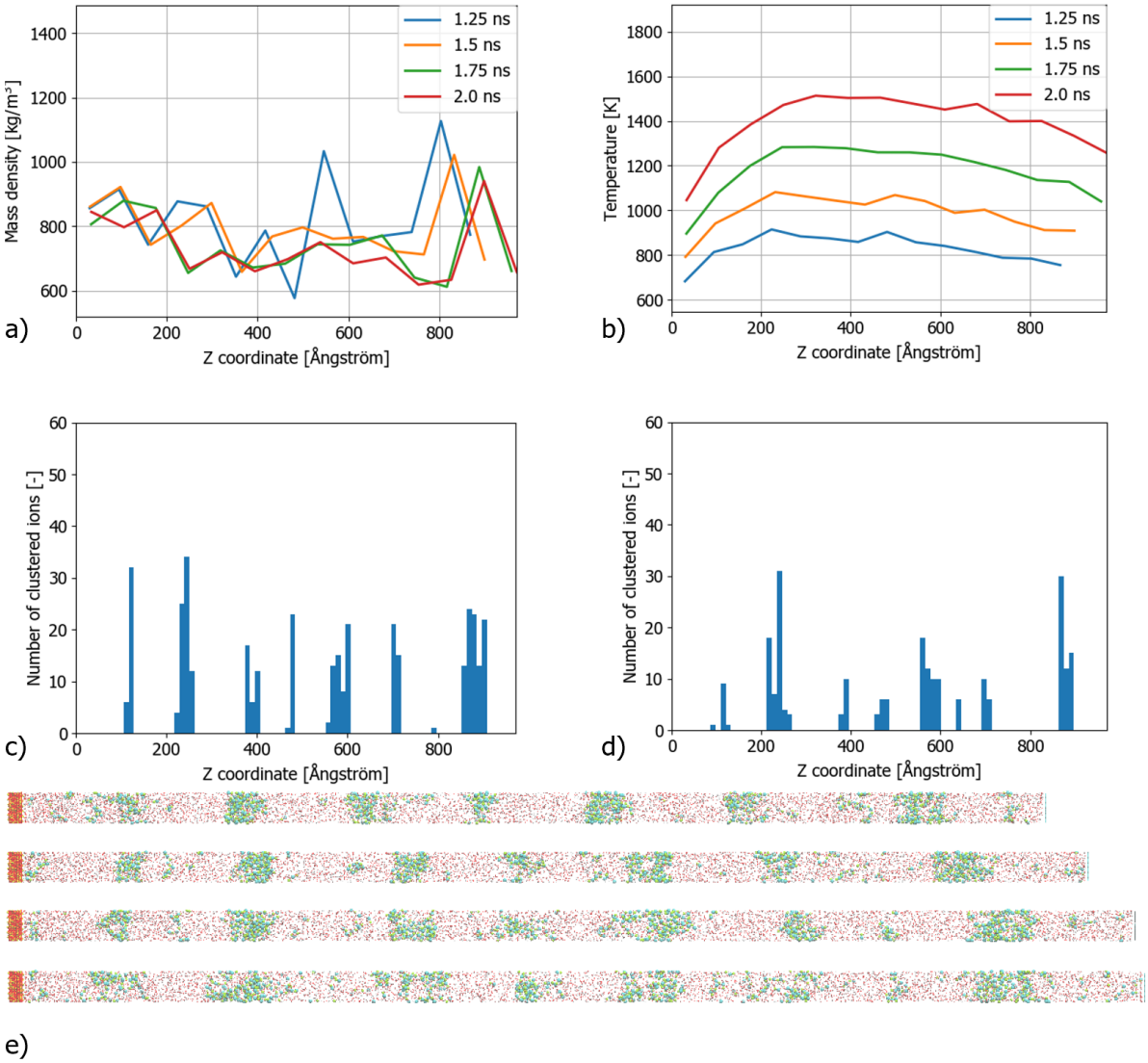

Figure 4.3: a) The density profiles at 4 instants, b) the temperature distributions at 4 instants, c) the number of clustered ions at $t = 1.5$ ns, d) the number of clustered ions at $t = 2$ ns and e) the system at $t = 1.25$ ns, $t = 1.5$ ns, $t = 1.75$ ns and $t = 2$ ns, respectively. The width of the bins is kept constant over the change in system size.

As can be seen in Figure 4.3, the density decreases further as the expansion proceeds. As the nanoparticle was

only heated to $T = 1500$ K, temperatures above 1500 K can only be obtained if a heat source is present. In this simulation, heat sources are provided by the clustering sites, where potential energy is converted into thermal energy during the clustering. Moreover, the amounts of thermal energy dissipated through the graphene thermostat are small compared to the amounts generated by the heat sources, which can be seen from the fact that the right hand side (RHS) of the system is hotter than the left hand side (LHS) at all of the temperature profiles. Inspection of Figure 4.3 e) shows that the system now contains a multitude of clusters in the shape of cuboids having $w > w_{\text{min}}$.

4.4. Cavitation Cycle

As completion of the cavitation cycle using adiabatic time evolution probably require simulation times which would be unfeasible for the given computational resources, it was decided to gradually cool the intermediate system back to $T = 298$ K and observe the behaviour of the ions. Specifically, a thermostat boundary was placed at $z = 1000$ Å such that a thermostat would be applied to the particles on the RHS of the boundary, whereas the thermostat would not be applied to the particles on the LHS of the boundary. Subsequently, the boundary was displaced towards $z = 0$ at a constant velocity for $t \in [1,5]$ ns. A pressure of $P = 4$ atm was also applied throughout the entire simulation. The results for the thermostat phase are found in Figure 4.4.

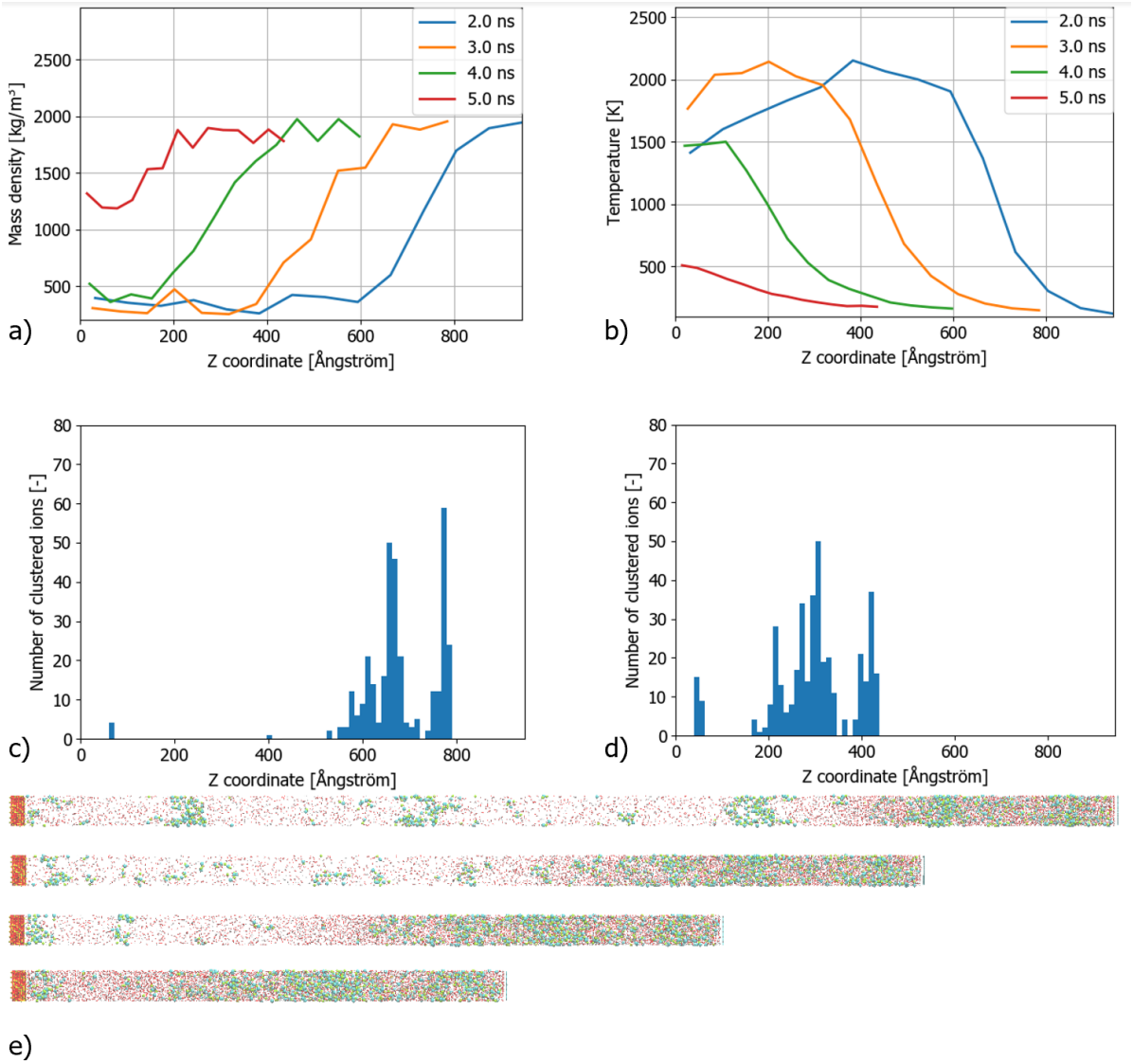

Figure 4.4: a) The density profiles at 4 instants, b) the temperature distributions at 4 instants, c) the number of clustered ions at $t = 3$ ns, d) the number of clustered ions at $t = 5.0$ ns and e) the system at $t = 2$ ns, $t = 3$ ns, $t = 4$ ns and $t = 5$ ns, respectively. The width of the bins is kept constant over the change in system size.

As can be seen in Figure 4.4 a), the column size decreased back to $z = 446$ Å and the concentration gradient now illustrates a more well-defined vapour-liquid interface. Moreover, the temperature is gradually reduced back towards $T = 298$ K in the final frames. In frames c) to e), it can be seen that the clusters have moved towards a region of higher total density, forming a large region of clustered ions. This observation is in agreement with the continuum approach, stating that the crystals should move out of the cavitation bubble. However, the NVT ensemble imposed on the system leads to somewhat artificial cooling, giving the ions insufficient time to rearrange into thermodynamically favourable configurations. Therefore, the current results do not allow for drawing decisive conclusions on the plausibility of the continuum approach.

4.5. Consequences of the system geometry

Some consequences of the columnar system geometry can now be evaluated.

As displayed in Figure 2.4, there is a significant difference in the temperature profiles between columnar and spherical geometries. This difference is reflected in the results as the amounts of thermal energy dissipated through the graphene thermostat are insufficient for completion of the cavitation cycle at time scales observed in MD simulations for spherical geometries [61]. Although part of the increase in the required simulation time can be attributed to the thermal energy produced by the clustering sites, it is expected that the cavitation cycle should complete significantly faster in a conically shaped region because of the quadratic proportionality between the thermostat area and the radius of the spherical system. Lastly, more cooling should occur in open systems compared to the closed system used in this paper of this paper, due to convection. For some of the simulations, several ion clusters spanned across the entire $\Delta x \Delta y$ plane, potentially inhibiting thermal diffusion.

Another consequence of the geometry is that clusters shaped as cuboids are more stable in the given geometry than spherical clusters. As a consequence, ΔG for the most stable configuration decreases. Because the nucleation rate according to the expression in Equation 1.4 depends exponentially on ΔG, less clustering may occur in simulations of a spherical geometry than the amount of clustering which has been found for the columnar geometry. Notably, the faces of the cuboid clusters tend to curve towards the fluid phase at the fluid-cluster interface, which suggests that $\delta > 0$ for KCl.

4.6. Evaluation of CICEN and CIPEN

Given the appearance of stable clusters in the system, the plausibility of CICEN and CIPEN can now be evaluated.

From the given results, it can be argued that CIPEN is not a likely mechanism for explaining cavity-induced nucleation. The argumentation is twofold. It has been shown in Section 3.2.3 that a laser intensity of $I = 10$ MW/(cm)^2 correlates to temperatures of $T = 1500$ K. From the results, it follows that applying such an intensity is sufficient for the clustering if ions. By contrast, it has been shown in Section 2.3.3 that such an intensity is still far below required intensities for significantly changing the chemical potential. Moreover, no well-defined vapour-liquid interface was observed in the density profiles, suggesting that no shockwave could have originated from any interface. Also, the density gradient $\Delta\rho/\Delta z$ is small in the first frames of the expansion phase, suggesting that the pressure gradient over the system is small. Therefore, the results are in agreement with the experimental observation that $I = 10$ MW/(cm)^2 is insufficient for the generation of shockwaves.

The second argument is based on the absence of a correlation between the z coordinate of originating clusters and the speed of presumed shockwaves. As the minimum shockwave velocity is equal to the velocity of sound in water v_{sound} [76], it could be argued that the clusters should start forming once the shockwave has traversed a clustering site. Taking $v_{\text{sound}} = 1500$ m/s at $T = 298$ K, a shockwave should traverse the system of $\Delta z = 500$ Å in a time of $\Delta t = 33$ ps. However, upon visually inspecting figures 4.1 c), d), 4.3 c), d) and e), it is found that the clusters in the LHS of the system start growing several hundreds of ps earlier than the clusters on the RHS. By contrast, there hardly be any visible correlation between the z coordinate and the cluster growth as there is a 250 ps time interval between all of the snapshots.

The different interpretations of the CICEN mechanism can now be evaluated at the molecular level. As has been shown in the results of Section 4.2, supercritical clusters start appearing at regions of high temperature, reflected in a local amount of clustered ions which has become approximately 3 times as high. Specifically, the clusters start to grow from the LHS towards the RHS as the density decreases in time. The subsequent evaporation of the solute molecules effectively traps the K^+ and Cl^-, making it favourable to cluster into larger structures. If the interfacial tension of a cluster-vapour interface is lower than the interfacial tension of a

cluster-liquid interface, the clusters in Figure 4.4 c) and d) should be found near the high density gradient in Figure 4.4 a). By contrast, the clusters are found largely in the liquid phase, suggesting that the vapour-liquid interface is of little relevance in nucleation near cavitation bubbles. Moreover, clusters are readily able to form before any vapour-liquid interface is well-defined. Therefore, the results point towards the CICEN interpretation in which ions are trapped due to local evaporation of the solvent. Moreover, there is no migration of the ions from the vapour into the liquid phase before the system is cooled, making it unlikely that the continuum approach applies for the entirety of the cavitation cycle. Referring to Figure 2.3, the clusters in the system are readily supercritical before the temperature in the any region decreases. Consequently, it is speculated that larger clusters may be obtained during the cavitation collapse as regions move further into the supersaturated regime, provided that the cavitation collapse is simulated while only cooling the system through thermostatting at the boundaries.

5

Conclusions & recommendations

In this chapter, the conclusions based on the theories and results are provided in Section 5.1 and the recommendations are provided in Section 5.2.

5.1. Conclusions

It has been shown using MD simulations that the heating of a nanoparticle leads to the clustering of K^+ and Cl^- ions in the vicinity of the nanoparticle, in agreement with previous MD simulations [15, 16]. Moreover, some of the clusters are supercritical ($\Delta G < 0$) and would correspond to nucleation in physical systems because they are found in regions where the NPT ensemble holds locally. The clustering of ions has been evaluated by using a bond order criterion [15]. The density of clustered ions increases by nearly an order of magnitude upon heating of the nanoparticle. The thermodynamic stability has been evaluated by considering whether $\Delta G < 0$ for the clusters, which requires cuboid clusters to have a width of $w > w_{\text{min}}$. Accordingly, many clusters were found to be stable for the columnar geometry.

The density of $\rho \approx 1500\ \text{kg/m}^3$ at $S(298\,\text{K})$ from the equilibrium system in this paper deviates significantly from the experimental density of superated KCl solutions of $\rho = 1180\ \text{kg/m}^3$ at $T = 298$ K [74]. The majority of the deviation is likely due to performing the simulations with the incorrect implementation of one or more force field parameters.

A complete cavitation cycle requires longer simulation time in a columnar geometry than in a spherical geometry. A single layer of graphene does not lead to dissipation of amounts of thermal energy comparable to the energies generated by the heating of the nanoparticle and the ion clustering sites.

More clustering should appear in a columnar geometry than in a spherical geometry because clusters shaped as rectangular cuboids with faces superimposed on the periodic boundaries are more stable than spherical clusters which will should in the absence of periodic boundaries. Consequently, ΔG in a columnar geometry is lower than ΔG in geometries where the clusters can span across the periodic boundaries. Clustering probabilities may be overestimated in columnar geometries because of the exponential dependence of the nucleation probability with ΔG.

It is unlikely that CIPEN is a relevant mechanism for NPLIN because of the laser intensities used in NPLIN experiments. Clusters appear in absence of a well-defined vapour-liquid interface, which is required for the generation of shockwaves. Moreover, there is no visible correlation between the distance of a hypothetical shockwave from the nanoparticle and the distance of the clustering sites from the nanoparticle.

The results suggest that CICEN is a plausible mechanism for nucleation. Specifically, the local solvent evaporation effectively traps the K^+ and Cl^- ions, leading to favourable cluster formation. The clusters are found to be stable before any cooling occurs, suggesting that the continuum assumption is not valid for describing nanoparticle heating mechanisms of NPLIN.

Although CICEN provides a plausible explanation for nucleation, a full description of NPLIN is still considered incomplete. DP provides a complete theoretical account of NPLIN and yields a strong correlation between predicted nucleation probabilities and experimental observations, without referring to the presence of nanoparticles. Moreover, there is no apparent explanation for obtaining particular polymorphs in the description of nanoparticle heating mechanisms.

5.2. Recommendations

The simulations of this paper should be repeated in a system with a conical geometry. In a conical geometry of sufficient size, the nanoparticle heating mechanisms can be studied without enhanced particle clustering through the periodic boundary conditions. Notably, there will be an increase in the surface area of the thermostat because of quadratic proportionality with the radius of the system, thereby providing higher dissipation of thermal energy. If the solid angle is large enough, spherical clusters will again be the most stable structure because clusters spanning across the entire surface area of the system will be less stable. The simulation of a complete cavitation cycle can be performed in less simulation time if the graphene layer is replaced by a material of higher conductivity in the direction perpendicular to the plane, allowing for dissipation of larger amounts of thermal energy. Such a geometry would probably no longer require imposed cooling of the solution molecules of the system studied in this paper.

To determine the influence of the OKE mechanism, the simulations should be repeated with anisotropically polarised molecules in the presence of an oscillating electric field. As the current configuration is readily able to induce clustering, such a system can be used to verify the change in the arrangement of clustered molecules. The influence of DP cannot be inferred from simulations using static charges, as used in the simulations from this paper.

The simulations may be repeated using metadynamics. If metadynamics are used, the stability of crystals can be observed rather than having to be inferred.

Bibliography

[1] William Humphrey, Andrew Dalke, and Klaus Schulten. VMD – Visual Molecular Dynamics. *Journal of Molecular Graphics*, 14:33–38, 1996.

[2] Thomas P van Waas. The mechanisms of non-photochemical laser-induced nucleation. Bachelor thesis, Delft University of Technology, 2019.

[3] André B de Haan and Hans Bosch. *Industrial separation processes: Fundamentals*. Walter de Gruyter, 2013.

[4] Lanny D Schmidt. *The engineering of chemical reactions*. Oxford University Press New York, 2005.

[5] BA Garetz, JE Aber, NL Goddard, RG Young, and AS Myerson. Nonphotochemical, polarization-dependent, laser-induced nucleation in supersaturated aqueous urea solutions. *Physical review letters*, 77(16):3475, 1996.

[6] Marco Nardone and Victor G Karpov. A phenomenological theory of nonphotochemical laser induced nucleation. *Physical Chemistry Chemical Physics*, 14(39):13601–13611, 2012.

[7] Stéphane Veesler, Kenji Furuta, Hiroaki Horiuchi, Hiroshi Hiratsuka, Natalie Ferté, and Tetsuo Okutsu. Crystals from light: photochemically induced nucleation of hen egg-white lysozyme. *Crystal growth & design*, 6(7):1631–1635, 2006.

[8] Bertrand Clair, Aziza Ikni, Wenjing Li, Philippe Scouflaire, Vincent Quemener, and Anne Spasojević-de Biré. A new experimental setup for high-throughput controlled non-photochemical laser-induced nucleation: application to glycine crystallization. *Journal of Applied Crystallography*, 47(4):1252–1260, 2014.

[9] Andrew J Alexander and Philip J Camp. Non-photochemical laser-induced nucleation. *The Journal of chemical physics*, 150(4):040901, 2019.

[10] Janice E Aber, Stephen Arnold, Bruce A Garetz, and Allan S Myerson. Strong dc electric field applied to supersaturated aqueous glycine solution induces nucleation of the γ polymorph. *Physical review letters*, 94(14):145503, 2005.

[11] Martin R Ward, Alasdair M Mackenzie, and Andrew J Alexander. Role of impurity nanoparticles in laser-induced nucleation of ammonium chloride. *Crystal Growth & Design*, 16(12):6790–6796, 2016.

[12] Richard P Sear. Nucleation: theory and applications to protein solutions and colloidal suspensions. *Journal of Physics: Condensed Matter*, 19(3):033101, 2007.

[13] Shufan Cai. The mechanism of cavitation bubble in non-photochemical laser induced nucleation. Masters thesis, Delft University of Technology, The Netherlands, 2019.

[14] Anamaria Soare, Rory Dijkink, Marcos Rodriguez Pascual, Chao Sun, Peter W Cains, Detlef Lohse, Andrzej I Stankiewicz, and Herman JM Kramer. Crystal nucleation by laser-induced cavitation. *Crystal growth & design*, 11(6):2311–2316, 2011.

[15] Julien O Sindt, Andrew J Alexander, and Philip J Camp. Effects of nanoparticle heating on the structure of a concentrated aqueous salt solution. *The Journal of chemical physics*, 147(21):214506, 2017.

[16] Julien O Sindt, Andrew J Alexander, and Philip J Camp. Structure and dynamics of potassium chloride in aqueous solution. *The Journal of Physical Chemistry B*, 118(31):9404–9413, 2014.

[17] Matteo Salvalaglio, Claudio Perego, Federico Giberti, Marco Mazzotti, and Michele Parrinello. Molecular-dynamics simulations of urea nucleation from aqueous solution. *Proceedings of the National Academy of Sciences*, 112(1):E6–E14, 2015.

[18] Johannes Lenhard. Computer simulation: The cooperation between experimenting and modeling. *Philosophy of Science*, 74(2):176–194, 2007.

[19] Margaret Morrison. Models, measurement and computer simulation: the changing face of experimentation. *Philosophical Studies*, 143(1):33–57, 2009.

[20] Michael P Allen and Dominic J Tildesley. *Computer simulation of liquids*. Oxford university press, 2017.

[21] M Scott Shell. *Thermodynamics and statistical mechanics: an integrated approach*. Cambridge University Press, 2015.

[22] Maria J Vesga, David McKechnie, Paul A Mulheran, Karen Johnston, and Jan Sefcik. Conundrum of γ glycine nucleation revisited: to stir or not to stir? *CrystEngComm*, 21(13):2234–2243, 2019.

[23] Tasfia Tasnim, Audrey Goh, Omar Gowayed, Chunhua T Hu, Tzu-Yi Chen, Janice E Aber, and Bruce A Garetz. Dendritic growth of glycine from nonphotochemical laser-induced nucleation of supersaturated aqueous solutions in agarose gels. *Crystal Growth & Design*, 18(10):5927–5933, 2018.

[24] Shubo Wang, Sumei Wang, Lan Jiang, Mengmeng Wang, Yuyin Wei, Jiaxin Sun, Shenghua Zhan, Xin Li, and Liangti Qu. Polymorph-controlled crystallization of acetaminophen through femtosecond laser irradiation. *Crystal Growth & Design*, 2019.

[25] Nadeem Javid, Thomas Kendall, Iain S Burns, and Jan Sefcik. Filtration suppresses laser-induced nucleation of glycine in aqueous solutions. *Crystal Growth & Design*, 16(8):4196–4202, 2016.

[26] Matthias Lenzner, Jörg Krüger, S Sartania, Z Cheng, Ch Spielmann, G Mourou, Wolfgang Kautek, and Ferenc Krausz. Femtosecond optical breakdown in dielectrics. *Physical review letters*, 80(18):4076, 1998.

[27] Jelena Matic, Xiaoying Sun, Bruce A Garetz, and Allan S Myerson. Intensity, wavelength, and polarization dependence of nonphotochemical laser-induced nucleation in supersaturated aqueous urea solutions. *Crystal growth & design*, 5(4):1565–1567, 2005.

[28] F_ Hache, D Ricard, Ch Flytzanis, and U Kreibig. The optical kerr effect in small metal particles and metal colloids: the case of gold. *Applied Physics A*, 47(4):347–357, 1988.

[29] Xiaoying Sun, Bruce A Garetz, and Allan S Myerson. Supersaturation and polarization dependence of polymorph control in the nonphotochemical laser-induced nucleation (nplin) of aqueous glycine solutions. *Crystal growth & design*, 6(3):684–689, 2006.

[30] Brandon C Knott, Jerry L LaRue, Alec M Wodtke, Michael F Doherty, and Baron Peters. Communication: Bubbles, crystals, and laser-induced nucleation, 2011.

[31] Mark D Cohen, Richard C Flagan, and John H Seinfeld. Studies of concentrated electrolyte solutions using the electrodynamic balance. 2. water activities for mixed-electrolyte solutions. *Journal of Physical Chemistry*, 91(17):4575–4582, 1987.

[32] Jihan Zhou, Yongsoo Yang, Yao Yang, Dennis S Kim, Andrew Yuan, Xuezeng Tian, Colin Ophus, Fan Sun, Andreas K Schmid, Michael Nathanson, et al. Observing crystal nucleation in four dimensions using atomic electron tomography. *Nature*, 570(7762):500, 2019.

[33] MD Luque De Castro and F Priego-Capote. Ultrasound-assisted crystallization (sonocrystallization). *Ultrasonics sonochemistry*, 14(6):717–724, 2007.

[34] Rohit Kacker, Sanjana Dhingra, Daniel Irimia, Murali Krishna Ghatkesar, Andrzej Stankiewicz, Herman JM Kramer, and Huseyin Burak Eral. Multiparameter investigation of laser-induced nucleation of supersaturated aqueous kcl solutions. *Crystal Growth & Design*, 18(1):312–317, 2017.

[35] Tibor Juhasz, George A Kastis, Carlos Suárez, Zsolt Bor, and Walter E Bron. Time-resolved observations of shock waves and cavitation bubbles generated by femtosecond laser pulses in corneal tissue and water. *Lasers in Surgery and Medicine: The Official Journal of the American Society for Laser Medicine and Surgery*, 19(1):23–31, 1996.

[36] Anvarbek Mukatovich Meirmanov. *The Stefan Problem*, volume 3. Walter de Gruyter, 2011.

[37] Anamaria Soare. Technologies for optimisation and control of nucleation and growth for new generations of industrial crystallizers. 2014.

[38] DA McQuarrie. Statistical mechanics. 2000. *Sausalito, Calif.: University Science Books*, 12:641, 2004.

[39] Daan Frenkel and Berend Smit. *Understanding molecular simulation: from algorithms to applications*, volume 1. Elsevier, 2001.

[40] Mark Tuckerman. *Statistical mechanics: theory and molecular simulation*. Oxford university press, 2010.

[41] Jos M Thijssen. *Computational physics*. Cambridge university press, 2007.

[42] Denis J Evans and Brad Lee Holian. The nose–hoover thermostat. *The Journal of chemical physics*, 83(8):4069–4074, 1985.

[43] Glenn J Martyna, Michael L Klein, and Mark Tuckerman. Nosé–hoover chains: The canonical ensemble via continuous dynamics. *The Journal of chemical physics*, 97(4):2635–2643, 1992.

[44] Edgar M Blokhuis and Joris Kuipers. Thermodynamic expressions for the tolman length. *The journal of chemical physics*, 124(7):074701, 2006.

[45] Ranjit Bahadur and Lynn M Russell. Effect of surface tension from md simulations on size-dependent deliquescence of nacl nanoparticles. *Aerosol Science and Technology*, 42(5):369–376, 2008.

[46] Orhan Ozdemir, Stoyan I Karakashev, Anh V Nguyen, and Jan D Miller. Adsorption and surface tension analysis of concentrated alkali halide brine solutions. *Minerals engineering*, 22(3):263–271, 2009.

[47] VM Yurov, SA Guchenko, and Mariya Sergeevna Gyngazova. Effect of an electric field on nucleation and growth of crystals. In *IOP Conference Series: Materials Science and Engineering*, volume 110, page 012019. IOP Publishing, 2016.

[48] Richard Haberman. *Applied partial differential equations: with Fourier series and boundary value problems*, volume 4. Pearson Prentice Hall Upper Saddle River, 2004.

[49] William J Cody. Rational chebyshev approximations for the error function. *Mathematics of Computation*, 23(107):631–637, 1969.

[50] The Engineering Toolbox (2018). Water - Thermal Diffusivity, 2018. Available: https://www.engineeringtoolbox.com/water-steam-thermal-diffusivity-d_2058.html [Accessed: 25 - Sep - 2019].

[51] Steve Plimpton. Fast parallel algorithms for short-range molecular dynamics. *Journal of computational physics*, 117(1):1–19, 1995.

[52] Sandia National Laboratories. LAMMPS version 5 Jun 2019. http://lammps.sandia.gov. [Computer software], Albuquerque, New Mexico, 2019.

[53] Andrew I Jewett, Zhuoyun Zhuang, and Joan-Emma Shea. Moltemplate a coarse-grained model assembly tool. *Biophysical Journal*, 104(2):169a, 2013.

[54] J Ewen and S Echeverri Restrepo. LAMMPS_Builder.

[55] James P Ewen, Sebastián Echeverri Restrepo, Neal Morgan, and Daniele Dini. Nonequilibrium molecular dynamics simulations of stearic acid adsorbed on iron surfaces with nanoscale roughness. *Tribology International*, 107:264–273, 2017.

[56] Python Software Foundation. Python Version 3.7.0. [Computer software], Dover, Delaware, 2019.

[57] Adobe Systems Incorporated. Adobe InDesign 2019. [Computer software], San José, California, 2019.

[58] Adobe Systems Incorporated. Adobe Premiere Pro 2019. [Computer software], San José, California, 2019.

[59] Adobe Systems Incorporated. Adobe Media Encoder 2019. [Computer software], San José, California, 2019.

[60] Robert B Corey and Linus Pauling. Molecular models of amino acids, peptides, and proteins. *Review of Scientific Instruments*, 24(8):621–627, 1953.

[61] Kiran Sasikumar and Pawel Keblinski. Molecular dynamics investigation of nanoscale cavitation dynamics. *The Journal of chemical physics*, 141(23):12B648_1, 2014.

[62] S Plimpton, A Thompson, S Moore, and A Kohlmeyer. Lammps documentation. *Sandia Corporation, Albuquerque, NM, accessed Apr*, 4:2019, 2019.

[63] Randall T Cygan, Jian-Jie Liang, and Andrey G Kalinichev. Molecular models of hydroxide, oxyhydroxide, and clay phases and the development of a general force field. *The Journal of Physical Chemistry B*, 108(4):1255–1266, 2004.

[64] Hassan Berro, Nicolas Fillot, and Philippe Vergne. Molecular dynamics simulation of surface energy and zddp effects on friction in nano-scale lubricated contacts. *Tribology international*, 43(10):1811–1822, 2010.

[65] Daniele Savio, Nicolas Fillot, Philippe Vergne, and Maurizio Zaccheddu. A model for wall slip prediction of confined n-alkanes: effect of wall-fluid interaction versus fluid resistance. *Tribology Letters*, 46(1):11–22, 2012.

[66] RL Blake, RE Hessevick, Tibor Zoltai, and Larry W Finger. Refinement of the hematite structure. *American Mineralogist: Journal of Earth and Planetary Materials*, 51(1-2):123–129, 1966.

[67] T Werder, Jens Honore Walther, RL Jaffe, T Halicioglu, and Petros Koumoutsakos. On the water- carbon interaction for use in molecular dynamics simulations of graphite and carbon nanotubes. *The Journal of Physical Chemistry B*, 107(6):1345–1352, 2003.

[68] HA Lorentz. Ueber die anwendung des satzes vom virial in der kinetischen theorie der gase. *Annalen der physik*, 248(1):127–136, 1881.

[69] HJC Berendsen, JR Grigera, and TP Straatsma. The missing term in effective pair potentials. *Journal of Physical Chemistry*, 91(24):6269–6271, 1987.

[70] R Saito, R Matsuo, T Kimura, G Dresselhaus, and MS Dresselhaus. Anomalous potential barrier of double-wall carbon nanotube. *Chemical physics letters*, 348(3-4):187–193, 2001.

[71] Stephen L Mayo, Barry D Olafson, and William A Goddard. Dreiding: a generic force field for molecular simulations. *Journal of Physical chemistry*, 94(26):8897–8909, 1990.

[72] Valentin A Levashov, Takeshi Egami, Rachel S Aga, and James R Morris. Equipartition theorem and the dynamics of liquids. *Physical review B*, 78(6):064205, 2008.

[73] Manuela Cavallari, Carlo Cavazzoni, and Mauro Ferrario*. Structure of nacl and kcl concentrated aqueous solutions by ab initio molecular dynamics. *Molecular Physics*, 102(9-10):959–966, 2004.

[74] David R Lide. *CRC handbook of chemistry and physics*, volume 85. CRC press, 2004.

[75] Neela Yennawar, Sava Denev, Venkataraman Gopalan, and Hemant Yennawar. Laser-improved protein crystallization screening. *Acta Crystallographica Section F: Structural Biology and Crystallization Communications*, 66(8):969–972, 2010.

[76] Chuanxi Wang and Veronica Eliasson. Shock wave focusing in water inside convergent structures. *The International Journal of Multiphysics*, 6(3), 2016.